Chemical Geology 383 (2014) 86–99

Contents lists available at ScienceDirect

Chemical Geology

journal homepage: www.elsevier.com/locate/chemgeo

Development of in situ sulfur four-isotope analysis with multiple Faraday cup detectors by SIMS and application to pyrite grains in a Paleoproterozoic glaciogenic sandstone

Takayuki Ushikubo [a,*], Kenneth H. Williford [a,b], James Farquhar [c], David T. Johnston [d], Martin J. Van Kranendonk [e], John W. Valley [a]

[a] WiscSIMS, Department of Geoscience, University of Wisconsin-Madison, Madison, WI 53706, USA
[b] Jet Propulsion Laboratory, California Institute of Technology, Pasadena, CA 91109, USA
[c] Department of Geology and Earth System Science Interdisciplinary Center, University of Maryland, College Park, MD 20742, USA
[d] Department of Earth and Planetary Sciences, Harvard University, Cambridge, MA 02138, USA
[e] School of Biological, Earth and Environmental Sciences, University of New South Wales, Kensington, NSW 2052, Australia

ARTICLE INFO

Article history:
Received 8 December 2013
Accepted 8 June 2014
Available online 17 June 2014

Editor: Michael E. Böttcher

Keywords:
Ion microprobe
SIMS
Sulfur isotope
S-MIF
Pyrite

ABSTRACT

An in situ sulfur four-isotope analysis technique with multiple Faraday cup detectors by ion microprobe was developed and applied to detrital pyrite grains in ~2.4 Ga glaciogenic sandstone from the Meteorite Bore Member of the Turee Creek Group, Western Australia. Data are standardized with the UWPy-1 pyrite standard ($\delta^{34}S = 16.04 \pm 0.18‰$, $\Delta^{33}S = -0.003 \pm 0.009‰$, and $\Delta^{36}S = -0.21 \pm 0.24‰$, 2 SD) whose sulfur four isotopes were newly determined by gas-source mass spectrometry. Typical reproducibility at two standard deviations (2 SD) of spot-to-spot analyses of standard UWPy-1 pyrite with a primary beam size of ~20 μm were ±0.23, ±0.05, and ±0.86‰ for $\delta^{34}S$, $\Delta^{33}S$, and $\Delta^{36}S$, respectively. The measured $^{36}S/^{32}S$ ratio [1 / (6641 ± 27)] is approximately 19‰ lower than the published ratio for VCDT, and we propose a revision of the ^{36}S abundance in VCDT.

Pyrite grains in ~2.4 Ga glaciogenic sandstone have wide ranging sulfur isotope ratios (−32.7 to 13.5 for $\delta^{34}S$, −3.03 to 11.66 for $\Delta^{33}S$, and −9.7 to 4.6 for $\Delta^{36}S$, respectively). Some pyrite grains are zoned in $\delta^{34}S$ values within a grain. Sulfur isotope ratios of most pyrite grains are distributed along a line with slope = −0.9 for $\Delta^{33}S$ vs. $\Delta^{36}S$, suggesting that pyrite grains mostly derived from a limited range of source rocks and near-surface sulfur reservoirs. One pyrite aggregate has a distinct texture from other pyrite grains in the same sandstone, and yields a significant mass-independent deficit in ^{36}S with a small excess in ^{33}S ($\Delta^{36}S/\Delta^{33}S$ ~ −4‰). This is used to suggest that this grain authigenically formed by biological activity during or after sedimentation. This work demonstrates that the use of multiple Faraday cup detectors provides improved accuracy and precision for in situ sulfur four-isotope analysis with secondary ion mass spectrometry.

© 2014 Elsevier B.V. All rights reserved.

1. Introduction

Sulfur four-isotope systematics of sulfur-bearing minerals in sedimentary rocks provides constraints on the evolution of the Earth's atmosphere and biological activity. Sulfur mass-independent fractionation (S-MIF), or deviation from the mass-dependent fractionation trends in $^{33}S/^{32}S$ and $^{36}S/^{32}S$ vs. $^{34}S/^{32}S$ ($\Delta^{33}S$ and $\Delta^{36}S$, respectively; see Section 3.1.2 for definitions), recorded in sedimentary rocks before ~2.4 Ga is generally interpreted to result from photochemical dissociation of volcanogenic SO_2 by ultraviolet light in an anoxic atmosphere (Farquhar et al., 2000; Pavlov and Kasting, 2002; Zahnle et al., 2006; Lyon, 2007; Danielache et al., 2008; Masterson et al., 2011; Whitehill and Ono, 2012; Ono et al., 2013; Whitehill et al., 2013). Another way to produce mass independent signatures is by chemistry occurring in liquid phase (Watanabe et al., 2009; Oduro et al., 2011; Kopf and Ono, 2012), but it is not clear if such mechanisms can account for the observed relationships among $\delta^{34}S$, $\Delta^{33}S$, and $\Delta^{36}S$, or account for the abundance of S-MIF in the Archean record (e.g., Kopf and Ono, 2012). One feature of the record that needs to be explained by any model for the origin of S-MIF is the observation of a change in slope for values of the $\Delta^{33}S$ vs. $\Delta^{36}S$ from about −0.9 to approximately −1.7 (Ono et al., 2006a, 2009a; Farquhar et al., 2007b, 2013; Kaufman et al., 2007; Zerkle et al., 2012; Thomazo et al., 2013).

Mass dependent fractionation of the more abundant sulfur isotopes ($\delta^{34}S$) by microbial sulfate reduction is suppressed to less than 6‰

* Corresponding author at: Kochi Institute for Core Sample Research, Japan Agency for Marine-Earth Science and Technology (JAMSTEC), 200 Monobe-otsu, Nankoku, Kochi 783-8502, Japan.
E-mail address: ushikubot@jamstec.go.jp (T. Ushikubo).

http://dx.doi.org/10.1016/j.chemgeo.2014.06.006
0009-2541/© 2014 Elsevier B.V. All rights reserved.

at sulfate concentrations less than 50 μmol, but it would increase at higher sulfate concentration and can be greater than 20‰ at sulfate concentrations higher than 200 μmol (Fig. 2(A) in Habicht et al., 2002). More recent observations of microbial sulfur isotope fractionation in a euxinic lake with sulfate concentrations of 100–350 μmol indicate that reservoir effects limit the degree to which larger (>20‰) kinetic fractionation effects are preserved in the rock record (Gomes and Hurtgen, 2013). Small variability in the $\delta^{34}S$ values of Archean sedimentary pyrite and expansion of variability in the $\delta^{34}S$ values of sedimentary pyrite after ~2.4 Ga are considered as the result of increasing concentration of seawater sulfate due to atmospheric oxygenation across the Great Oxygenation Event (GOE: Holland, 1984, 1994; Bekker et al., 2004; Canfield, 2005; Papineau et al., 2007; Partridge et al., 2008; Guo et al., 2009; Williford et al., 2011).

Sedimentary pyrite forms by multiple processes that are reflected in sulfur isotope signatures of individual pyrite grains. For example, Partridge et al. (2008) found that fine-grained pyrite in Neoarchean sedimentary rocks in the Hamersley Basin, Western Australia has positive $\Delta^{33}S$ values but that pyrite nodules in the same sedimentary rocks have negative $\Delta^{33}S$ values. Ono et al. (2009a) reported that $\Delta^{33}S$ and $\Delta^{36}S$ values of disseminated pyrite grains were distinct from those of pyrite nodules and layered pyrites in the same samples of 2.5 Ga Klein Naute Formation, South Africa. Furthermore, Williford et al. (2011) used a 3 μm diameter SIMS beam to show that many pyrite grains from glaciogenic mudstone and sandstone of the ~2.4 Ga Meteorite Bore Member of Western Australia are zoned with biogenic cores having low $\delta^{34}S$ values (<−20‰) and thin (≤10 μm) diagenetic or hydrothermal overgrowths with ~30‰ higher $\delta^{34}S$ values (4 to 7‰). This study showed that in situ sulfur isotope analyses with micrometer-scale spatial resolution provide additional information to investigate the signatures of multiple processes and multiple sulfur sources for pyrite formation, such as input of elemental sulfur aerosols, microbial sulfate reduction, and deposition by later hydrothermal activity (Williford et al., 2011; Philippot et al., 2012; Johnson et al., 2013).

In situ sulfur isotope analysis by the ion microprobe is a powerful technique to observe intra- and inter-grain sulfur isotope variability of a few to tens of μm-scale in sedimentary pyrite (Deloule et al., 1986; Graham and Valley, 1992; Farquhar et al., 2002, 2013; Mojzsis et al., 2003; Whitehouse et al., 2005; Kamber and Whitehouse, 2007; Papineau et al., 2007; Fayek, 2009; Kozdon et al., 2010; Williford et al., 2011; Roerdink et al., 2013; Whitehouse, 2013). Although it is recognized that sphalerite and galena exhibit crystal orientation effects which cause a significant change of the instrumental bias for the $\delta^{34}S$ value corresponding to crystal orientation (e.g., Kozdon et al., 2010; Kita et al., 2011), Kozdon et al. (2010) showed that using the same sulfur two-isotope technique as applied in this study, no significant crystal orientation effects exist for analysis of pyrite, chalcopyrite, and pyrrhotite beyond the reproducibility of spot-to-spot analyses of a single grain. Thus, no correction for crystal orientation effect is required for the sulfur isotope analysis of these three minerals.

In this study, we developed an ion microprobe technique for sulfur four-isotope analysis of pyrite with simultaneous detection by four Faraday cup (FC) detectors. In most other studies, in situ sulfur four-isotope analysis used an electron multiplier (EM) to measure the least abundant sulfur isotope, ^{36}S (Farquhar et al., 2013; Roerdink et al., 2013; Whitehouse, 2013). However, there are two important benefits to using a FC detector for the $^{36}S^{-}$ signal. First, relative efficiency between two FC detectors is more stable than that between a FC detector and an EM detector. In particular, if an EM detector is used to measure ions whose count rate is higher than a few hundred thousand counts per second (cps), the aging effect (decrease of detection efficiency) of the EM detector is critical. The decrease of EM detector efficiency will change the measured isotope ratios and must be carefully monitored. Second, the upper limit of count rate for an EM (<several hundred thousands cps) prevents the use of a strong primary beam current and reduces the attainable analytical precision for the three other sulfur isotopes that are measured by FC detectors. Modification of a Faraday cup detection system (replacing a feedback resister with a capacitor, Ireland et al., 2014) provides further opportunity for improvement of precision of sulfur four-isotope analysis.

Reproducibility of the sulfur four-isotope analyses ($\delta^{34}S$, $\Delta^{33}S$, and $\Delta^{36}S$) was evaluated using the pyrite standards, UWPy-1 (Kozdon et al., 2010) and Ruttan pyrite (Crowe and Vaughan, 1996; Cabral et al., 2013). This technique was also applied to measure sulfur four-isotope ratios of detrital pyrite grains in the glaciogenic sandstone, MB190583, from Williford et al. (2011). Williford et al. (2011) performed sulfur three-isotope analyses of sedimentary pyrite grains from multiple layers in exposures of the uppermost Hamersley Group and the lowermost Turee Creek Group at the Boundary Ridge and Deepdale localities, Western Australia (~2.4 Ga; Martin, 1999; Van Kranendonk, 2010). Williford et al. (2011) recognized that the glaciogenic sandstone (MB190583) layer contained abundant detrital pyrite grains with a wide range of $\Delta^{33}S$ values (−3.6 to 11.7‰), which were more variable than the authigenic pyrite grains of neighboring beds (typically −1 to 1‰). Results of sulfur four-isotope analyses of the same detrital pyrite grains analyzed for sulfur 3-isotope ratios by Williford et al. (2011) will be presented. Repeated measurements with a new analytical protocol for sulfur four-isotopes provide an opportunity to evaluate reproducibility of results by different analytical conditions and place further constraints on the origin of pre-GOE detrital pyrite grains in this glaciogenic sandstone.

2. Samples

2.1. Pyrite standards

The UWPy-1 pyrite standard (Kozdon et al., 2010) is coarse grained and homogeneous due to upper amphibolite facies recrystallization of the Mesoproterozoic Balmat massive sulfide deposit. UWPy-1 was used as a running standard for all sulfur isotope analysis sessions in this study. Sulfur four-isotope ratios of UWPy-1 have been determined using bulk analysis techniques that converted them to SF_6, which was measured using gas-source mass spectrometry at the University of Maryland and Harvard University (Table 1). Individual analysis data are provided in Table S1 in Electronic Annex. In this study, the newly determined sulfur isotope ratios of UWPy-1 were used. Sulfur isotope ratios of Ruttan pyrite (~1.88 Ga, $\delta^{34}S = 1.2$ to 1.4‰, Crowe and Vaughan, 1996; Barrie and Taylor, 2001; Cabral et al., 2013) were also measured by ion microprobe. Although we did not determine sulfur four-isotope ratios of Ruttan pyrite by gas-source mass spectrometry in this study, no detectable S-MIF signature in Ruttan pyrite was reported ($\Delta^{33}S = -0.003 \pm 0.012$, 2σ, Cabral et al., 2013) and its formation age is at least 400 Ma younger than GOE. For these reasons, we assume that the Ruttan pyrite we used does not have S-MIF signature larger than reproducibility by ion microprobe analyses.

2.2. Detrital Paleoproterozoic pyrite grains in glaciogenic sandstone

Sample MB190583 (sample 5 in Williford et al., 2011) is a glaciogenic sandstone with abundant detrital quartz and pyrite grains from the Meteorite Bore Member of the Turee Creek Group at the Boundary Ridge locality, Western Australia (Van Kranendonk, 2010; Williford et al., 2011). Two rock chips (~1 cm in size) of the sandstone were mounted in a 2.5 cm diameter epoxy disk with the pyrite standard UWPy-1 near the center. Most pyrite grains measured in this study were analyzed for sulfur three-isotope ratios by Williford et al. (2011). The sample mount was lightly ground and repolished to remove previous analysis pits (~1 μm in depth) and the new surface of each grain was checked by SEM before sulfur four-isotope analysis.

Most pyrite grains in MB190583 are 10 to 200 μm in size and have either rounded or irregular anhedral shapes (Fig. 1a–d). Pyrite grains with subhedral shape are rare (Fig. 1e). A single pyrite aggregate, g9,

Table 1
Sulfur four-isotope ratios of the standard sulfide, UWPy-1 measured by conversion of powdered sample to SF_6 and gas-source mass spectrometry.

	$\delta^{33}S$ (‰ VCDT)	2 SD	$\delta^{34}S$ (‰ VCDT)	2 SD	$\delta^{36}S$ (‰ VCDT)	2 SD	$\Delta^{33}S$ (‰)	2 SD	$\Delta^{36}S$ (‰)	2 SD
Maryland (n = 6)[a]	8.20	±0.14	16.00	±0.28	30.69	±0.54	−0.006	±0.016	−0.01	±0.40
Harvard (n = 6)	8.25	±0.12	16.08	±0.23	30.37	±0.43	−0.001	±0.008	−0.40	±0.27
Average	8.23	±0.09	16.04	±0.18	30.53	±0.34	−0.003	±0.009	−0.21	±0.24

[a] Long-term reproducibilities at stable isotope laboratory of University of Maryland are assigned as analysis uncertainties.

consisting of subhedral pyrite grains (~10 μm diameter) was observed (Fig. 1f). Some pyrite grains contain silicate inclusions (mostly quartz and K-feldspar, which are abundant in the sandstone, Fig. 1b). We did not observe evidence for multiple domains in the samples studied by SEM. Backscattered electron (BSE) images of individual pyrite grains and analysis pit positions are shown in Figure S1 in Electronic Annex.

3. Methods

3.1. Simultaneous sulfur four-isotope analysis with multiple Faraday cups (sessions 1 and 4)

3.1.1. Analytical conditions

Sulfur four-isotope analyses were conducted using a CAMECA ims-1280 large radius multi-collector ion microprobe at the WiscSIMS Laboratory, University of Wisconsin-Madison. After modifications of the ims-1280 detector assembly that are described below, analysis procedures were similar to those previously reported for sulfur two-isotope (^{32}S and ^{34}S) analyses (Kozdon et al., 2010) and sulfur three-isotope (^{32}S, ^{33}S, and ^{34}S) analyses (Williford et al., 2011).

To perform in situ measurements of sulfur four-isotopes (^{32}S, ^{33}S, ^{34}S, and ^{36}S), a primary $^{133}Cs^+$ ion beam with an intensity of 4.5 to 5.3 nA and a total impact energy of 20 kV was focused to approximately 20 μm in diameter at the surface of the sample. A slightly defocused Gaussian beam was used to achieve a high density and a nearly homogeneous primary beam condition. A gold coat of ~30 nm thickness was applied on the sample surface and a normal-incidence electron gun was used for charge compensation. Secondary ions of the four sulfur isotopes were accelerated at 10 kV and detected simultaneously by four Faraday cups. A FC detector with a 10^9 Ω resistor was used to measure $^{32}S^-$ at the L′2 position, and FC detectors with 10^{11} Ω resistors were used to measure $^{33}S^-$, $^{34}S^-$, and $^{36}S^-$ ions at L1, H1, and H′2 positions, respectively (see Fig. 1c in Kita et al., 2009).

For sulfur four-isotope analysis, a mass resolving power (MRP, M/ΔM at 10% peak height) of >4000 is required to eliminate a tailing interference signal of the $^{32}SH^-$ peak from the $^{33}S^-$ signal. In contrast, a MRP of ~2200 is desirable to obtain wide flat peak tops of the mass spectrum for $^{32}S^-$, $^{34}S^-$, and $^{36}S^-$ ions. The standard ims-1280 exit slit plate has three vertically aligned slits with widths of 500 μm, 250 μm, and 150 μm at slit positions #1, #2, and #3, respectively. Different MRP can be achieved by changing the slit positions. However, due to a limitation of the normal ims-1280 multi-collector system, the slit positions of all FC detectors in the multiple collector system must be same and different MRP cannot be set for individual FC detectors. Because shape of mass spectrum tends to be deformed at a place distant from the optic axis, unnecessary high MRP settings with narrow exit slit width for $^{32}S^-$ and $^{36}S^-$ measurements make difficult to achieve a higher transmission of the ions with a wider entrance slit width. To achieve different MRP settings, modified exit slit plates which have slits with widths of 500 μm, 500 μm, and 150 μm at slit positions #1, #2, and #3, respectively, were installed before the L′2 and H′2 FC detectors (for $^{32}S^-$ and $^{36}S^-$ measurements, respectively). All exit slit positions were set at #2. MRPs of individual detectors were ~2200 for $^{32}S^-$ (L′2) and $^{36}S^-$ (H′2) with a 500 μm width exit slit (modified exit slit plate), and ~5000 for $^{33}S^-$ (L1) and $^{34}S^-$ (H1) with a 250 μm width exit slit (the standard exit slit plate), respectively. This modification improves count rates of sulfur ions and stability of analysis conditions with sub-permil precision for all sulfur isotope ratios significantly. To achieve these MRP settings, modified exit slit plates were installed before the L′2 and H′2 FC detectors ($^{32}S^-$, $^{36}S^-$, respectively). This modification is required because the standard ims-1280 exit slit plate has three vertically aligned slits with widths of 500 μm, 250 μm, and 150 μm at slit positions #1, #2, and #3, respectively. Different MRP can be achieved by changing the slit positions. Due to a

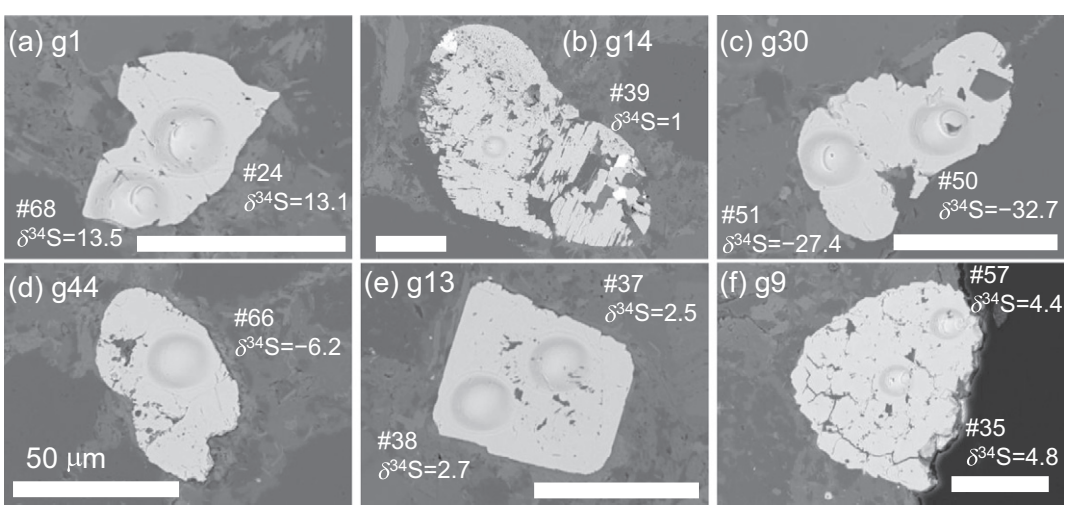

Fig. 1. Backscattered electron (BSE) images of typical detrital pyrite grains in the 2.4 Ga glaciogenic sandstone from the Meteorite Bore Member of the Turee Creek Group MB190583, after sulfur four-isotope analyses by SIMS. Rounded or irregular anhedral shape pyrite grains: (a) g1, (b) g14, (c) g30, and (d) g44, (e) a subhedral pyrite grain g13, (f) a pyrite aggregate g9. The numbers in the images correspond to the analysis #s in Table 1. The $\delta^{34}S$ value for each analysis is also shown. Scale bars indicate 50 μm.

limitation of the normal ims-1280 multi-collector system, the slit positions of all FC detectors in the multiple collector system must be the same and different slit positions cannot be set for individual FC detectors. The modified exit slit plate used in this study has 500 μm, 500 μm, and 150 μm at slit positions #1, #2, and #3, respectively (for L′2 and H′2 detectors). All exit slit positions were set at #2 and obtained different MRP for individual FC detectors. MRPs of individual detectors were set to ~2200 for $^{32}S^-$ (L′2) and $^{36}S^-$ (H′2) with a 500 μm width exit slit (position #2 of the modified exit slit plate), and ~5000 for $^{33}S^-$ (L1) and $^{34}S^-$ (H1) with a 250 μm width exit slit (position #2 of the standard exit slit plate), respectively.

Each analysis consisted of 10 seconds (s) for pre-sputtering, 80 s for centering of secondary ions to the field aperture, and 80 s for measurement. Average count rates for $^{32}S^-$ confirmed stability of individual analyses. A typical count rate of $^{32}S^-$ signal was ~5×10^9 counts per second (cps) for pyrite analyses. To monitor the magnitude of interference from $^{32}SH^-$ to the $^{33}S^-$ signal, the $^{32}SH^-$ peak was measured after each analysis by scanning the deflector that is located between the electromagnet analyzer and the FC detectors (Heck et al., 2010; Williford et al., 2011). The ratio of the $^{32}SH^-$ tail at the $^{33}S^-$ peak position relative to the $^{32}SH^-$ peak ($^{32}SH-_{tail}/^{32}SH^-_{peak}$) was determined to be ~$1 \times 10^{-5}$ in the same session, and this ratio and the $^{32}SH^-$ peak count rate were used to correct the contribution of the $^{32}SH^-$ tail signal to the $^{33}S^-$ peak. A typical count rate of $^{32}SH^-$ peak signal of the samples was 1.2×10^7 cps and the height of the tail under the ^{33}S peak was about 100 cps. Thus, correction for $^{32}SH^-$ contribution to the $^{33}S^-$ peak (~4.1×10^7 cps) was less than 0.01‰ (Table S4 in Electronic Annex), which is negligible relative to the spot-to-spot reproducibility (typically ±0.05‰, 2 SD in $\Delta^{33}S$).

3.1.2. Sulfur isotope data reduction

Every five to 12 analyses of pyrite samples were bracketed by a total 8 to 10 standard UWPy-1 analyses. Instrumental biases and analytical reproducibility for $\delta^{34}S$, $\Delta^{33}S$, and $\Delta^{36}S$ of pyrite samples were determined by average values and 2 SD of these bracketing standard analyses (Valley and Kita, 2009; Williford et al., 2011).

The methods for the data reduction were similar to the sulfur three-isotope analyses by Williford et al. (2011). Measured ratios of $^{34}S/^{32}S$, $^{33}S/^{32}S$, and $^{36}S/^{32}S$ were divided by Vienna Canyon Diablo Troilite (VCDT) values ($^{34}S/^{32}S = 1/22.6436$, $^{33}S/^{32}S = 1/126.948$, and $^{36}S/^{32}S = 1/6515$, Ding et al., 2001) and were calculated as "raw" δ-values, $\delta^{34}S_{raw}$, $\delta^{33}S_{raw}$, and $\delta^{36}S_{raw}$, respectively. Correction for $^{32}SH^-$ contribution to the $^{33}S^-$ peak was applied at this step. In this study, equations of mass-dependent fractionation of sulfur isotopes were employed:

$$\delta^{i}S(\text{unknown}) = \left\{\left(^{i}S/^{32}S\right)_{\text{unknown}}/\left(^{i}S/^{32}S\right)_{\text{VCDT}} - 1\right\} \times 1000$$
$$\left(1 + \delta^{33}S/1000\right) = \left(1 + \delta^{34}S/1000\right)^{0.515}$$
$$\left(1 + \delta^{36}S/1000\right) = \left(1 + \delta^{34}S/1000\right)^{1.9}$$

where i = 33, 34, or 36 (Farquhar et al., 2007a).

Correction factors of the instrumental bias of $\delta^{34}S$, $\Delta^{33}S$, and $\Delta^{36}S$ for pyrite measurements were determined using $\delta^{34}S_{raw}$, $\delta^{33}S_{raw}$, and $\delta^{36}S_{raw}$ values of bracketing analyses of UWPy-1 ($\delta^{34}S = 16.04$‰ VCDT, $\Delta^{33}S = 0.00$‰, and $\Delta^{36}S = -0.21$‰, Table 1) as follows:

$$\alpha_{SIMS}(\text{pyrite}) = \left\{1 + \delta^{34}S_{raw}(\text{UWPy-1})/1000\right\}/1.01604 \quad (1)$$

$$\text{Bias}\left(\Delta^{33}S\right) \equiv \Delta^{33}S_{raw}(\text{UWPy-1}) \quad (2)$$

where $\Delta^{33}S_{raw}(\text{UWPy-1}) = \delta^{33}S_{raw}(\text{UWPy-1}) - 1000 \times \{(1 + \delta^{34}S_{raw}(\text{UWPy-1})/1000)^{0.515} - 1\}$

$$\text{Bias}\left(\Delta^{36}S\right) \equiv \Delta^{36}S_{raw}(\text{UWPy-1}) + 0.21 \quad (3)$$

where $\Delta^{36}S_{raw}(\text{UWPy-1}) = \delta^{36}S_{raw}(\text{UWPy-1}) - 1000 \times \{(1 + \delta^{34}S_{raw}(\text{UWPy-1})/1000)^{1.9} - 1\}$.

Values of $\delta^{34}S$, $\Delta^{33}S$, and $\Delta^{36}S$ of pyrite samples were calculated using measured values of pyrite samples and correction factors as follows:

$$\delta^{34}S(\text{sample}) = 1000 \times \left\{\left(1 + \delta^{34}S_{raw}(\text{sample})/1000\right)/\alpha_{SIMS}(\text{pyrite}) - 1\right\} \quad (4)$$

$$\Delta^{33}S(\text{sample}) = \delta^{33}S_{raw}(\text{sample}) - 1000 \times \left\{\left(1 + \delta^{34}S_{raw}(\text{sample})/1000\right)^{0.515} - 1\right\} - \text{Bias}\left(\Delta^{33}S\right) \quad (5)$$

$$\Delta^{36}S(\text{sample}) = \delta^{36}S_{raw}(\text{sample}) - 1000 \times \left\{\left(1 + \delta^{34}S_{raw}(\text{sample})/1000\right)^{1.9} - 1\right\} - \text{Bias}\left(\Delta^{36}S\right) \quad (6)$$

The same correction factors of $\Delta^{33}S$ and $\Delta^{36}S$ were applied for pyrite samples that have a different $\delta^{34}S$ value. This assumption is supported by analyses of the two standard pyrites UWPy-1 and Ruttan pyrite (see Section 4.1.1).

3.2. Additional experimental tests for ^{36}S

In this study, large apparent instrumental bias for $^{36}S/^{32}S$ (Bias($\Delta^{36}S$)) of approximately −20‰ (see Section 4.1.1) was consistently obtained. Large apparent instrumental biases (approximately −30‰) for $^{36}S/^{32}S$ were also observed by Farquhar et al. (2013) and Roerdink et al. (2013) (e.g. Table S1 for Farquhar et al., 2013 and Tables S1 and S2 for Roerdink et al., 2013, respectively) although it is difficult to compare these values to those in this study because of different detector settings (an EM detector was used to measure $^{36}S^-$ signal in previous studies but all sulfur four-isotope signals were measured by FC detectors in this study). To understand the cause of this anomalously large instrumental bias for ^{36}S, additional tests (sessions 2 and 3) were performed. Here, we briefly describe the new analysis settings and the purpose of these tests. Detailed descriptions of experimental tests are provided in Electronic Annex.

3.2.1. Oxygen two-isotope test analysis (session 2)

Because a measured large apparent instrumental bias for $^{36}S/^{32}S$ might be caused by lower sensitivity of the H′2 FC detector, which was used to detect $^{36}S^-$ ions, relative to other FC detectors, oxygen two-isotope analyses of the quartz standard UWQ-1 ($\delta^{18}O = 12.33$‰ VSMOW, Kelly et al., 2007) were performed to evaluate relative sensitivity between H1 and H′2 FC detectors with two different detector configurations: (1) the L′2 (10^{10} Ω resistor for $^{16}O^-$) and H1 (with 10^{11} Ω resistor for $^{18}O^-$) FC detector settings, and (2) the L′2 ($^{16}O^-$) and H′2 (10^{11} Ω resistor for $^{18}O^-$) FC detector settings. If a lower sensitivity of the H′2 FC detector was the cause of the large apparent instrumental bias for $^{36}S/^{32}S$, detectable change was expected in results of oxygen two-isotope analyses with configurations (1) and (2).

Further analytical conditions of session 2 are provided in section S1 in Electronic Annex. Results are shown in Section 4.1.2.

3.2.2. Sulfur isotope analysis with the axial FC2 Faraday cup detector and peak-switching mode (session 3)

Additional analyses of only the three less abundant sulfur isotopes ($^{33}S^-$, $^{34}S^-$, and $^{36}S^-$) of UWPy-1 were performed using the axial FC2 detector (Faraday cup with 10^{11} Ω resistor) operated by magnetic peak switching. In this session, the major isotope ^{32}S signal was not measured because the count rate of $^{32}S^-$ ions exceeded the detection

Table 2
Raw sulfur four-isotope ratios of sulfide standards at WiscSIMS.

Mineral, analysis #	Order in Fig. 2[a]	$\delta^{34}S_{raw}$ (‰)	2 SD	α[b]	$\delta^{33}S_{raw}$[c] (‰)	2 SD	$\delta^{36}S_{raw}$ (‰)	2 SD	$\Delta^{33}S_{raw}$ (‰)	2 SD	$\Delta^{36}S_{raw}$ (‰)	2 SD	$^{32}SH^-$ tail[d] (‰)	$^{32}S^-$ count rate (cps)	I[e] (nA)	$^{32}S^-$ yield (10^9 cps/nA)
UWPy-1 (Balmat pyrite)																
(Session 1)																
#5–8, n = 4	1	17.68	±0.35	1.0016	9.53	±0.17	13.04	±0.58	0.47	±0.03	−20.81	±0.46	0.00023	5.01E+09	4.20	1.19
#13–16, n = 4	2	17.58	±0.04	1.0015	9.49	±0.03	12.67	±1.27	0.47	±0.02	−21.00	±1.30	0.00022	5.18E+09	4.37	1.18
#33–36, n = 4	4	17.41	±0.39	1.0013	9.38	±0.24	12.59	±1.38	0.46	±0.04	−20.74	±0.65	0.00019	5.26E+09	4.56	1.15
(Session 4)																
#5–9, 14–17, n = 9	6	18.43	±0.05	1.0024	9.89	±0.05	15.38	±1.23	0.44	±0.04	−19.94	±1.24	0.00021	5.07E+09	4.55	1.11
#18–23, 29–32, n = 10	7	18.28	±0.27	1.0022	9.83	±0.14	14.98	±1.02	0.45	±0.03	−20.05	±1.01	0.00093	5.59E+09	5.16	1.08
#29–32, 40–43, n = 8	8	18.30	±0.42	1.0022	9.84	±0.21	15.46	±0.93	0.46	±0.03	−19.60	±0.64	0.00101	5.67E+09	5.21	1.09
#40–43, 53–56, n = 8	9	18.49	±0.39	1.0024	9.94	±0.21	16.02	±1.35	0.46	±0.06	−19.40	±1.11	0.00106	5.72E+09	5.26	1.09
#53–56, 69–72, n = 8	10	18.60	±0.17	1.0025	9.98	±0.13	16.07	±1.20	0.44	±0.06	−19.57	±1.25	0.00106	5.73E+09	5.27	1.09
#75–78, 89–92, n = 8	11	18.60	±0.44	1.0025	9.98	±0.28	15.18	±1.05	0.44	±0.07	−20.46	±0.95	0.00098	5.65E+09	5.27	1.07
#89–92, 102–105, n = 8	12	18.69	±0.52	1.0026	10.03	±0.32	15.64	±1.36	0.45	±0.06	−20.17	±0.94	0.00095	5.69E+09	5.26	1.08
#102–105, 116–119, n = 8	13	18.84	±0.10	1.0028	10.12	±0.07	16.23	±0.36	0.46	±0.04	−19.87	±0.41	0.00096	5.60E+09	5.21	1.07
#116–119, 125–128, n = 8	14	18.88	±0.07	1.0028	10.15	±0.06	16.34	±0.65	0.47	±0.06	−19.83	±0.62	0.00093	5.54E+09	5.14	1.08
#131–134, 143–146, n = 8	15	18.79	±0.44	1.0027	10.09	±0.25	16.07	±1.85	0.46	±0.05	−19.93	±1.16	0.00102	5.35E+09	5.31	1.01
#147–150, 159–162, n = 8	16	19.06	±0.14	1.0030	10.22	±0.09	16.31	±0.73	0.45	±0.04	−20.20	±0.84	0.00176	5.61E+09	5.16	1.09
#163–166, 176–179, n = 8	17	19.11	±0.12	1.0030	10.27	±0.06	16.54	±0.77	0.47	±0.02	−20.09	±0.63	0.00138	5.75E+09	5.32	1.08
#182–185, 194–197, n = 8	18	19.23	±0.15	1.0031	10.33	±0.06	16.50	±0.76	0.47	±0.03	−20.35	±0.70	0.00050	5.66E+09	5.22	1.08
#207–210, 221–224, n = 8	19	19.33	±0.10	1.0032	10.36	±0.07	17.10	±0.57	0.45	±0.04	−19.94	±0.56	0.00026	5.53E+09	5.25	1.05
#221–224, 230–233, n = 8	20	19.32	±0.08	1.0032	10.36	±0.06	17.08	±0.67	0.46	±0.05	−19.94	±0.64	0.00028	5.38E+09	5.11	1.05
#236–239, 249–252, n = 8	21	19.31	±0.23	1.0032	10.37	±0.11	17.16	±1.31	0.47	±0.05	−19.85	±1.33	0.00008	5.33E+09	5.09	1.05
#253–256, 267–270, n = 8	22	19.42	±0.25	1.0033	10.43	±0.12	17.08	±0.71	0.47	±0.05	−20.14	±0.65	0.00067	5.66E+09	5.34	1.06
Average 2SD of session 4			±0.23							±0.05		±0.86				
Ruttan pyrite																
(Session 1)																
#21–24, n = 4	3	2.91	±0.34	1.0017	1.96	±0.19	−15.23	±1.35	0.47	±0.04	−20.76	±1.03	0.00017	5.04E+09	4.38	1.15
(Session 4)																
#10–13, n = 4	5	3.63	±0.48	1.0024	2.32	±0.21	−12.50	±1.08	0.45	±0.04	−19.41	±0.57	0.00020	5.14E+09	4.55	1.13

[a] Order of data shown in Fig. 2 starting from left.
[b] The α is defined by the formula (1) in the Section 3.1.2.
[c] Interference signal from the $^{32}SH^-$ is corrected.
[d] Amounts of correction (in ‰) of the interference $^{32}SH^-$ signal to the $^{33}S^-$ signal.
[e] The Cs^+ primary beam intensity.

limit the detector. Because sulfur isotopes were detected by the same detector at the axial position of the secondary ion optics, results of these test analyses have no affect on different sensitivity among multiple detectors or different trajectories of measured ions.

The baseline of the FC2 detector after detection of the ^{34}S signal was also measured because change of the detector's baseline could affect measurements of ^{36}S signal. Further information and analytical conditions of session 3 are provided in section S2 in Electronic Annex. Results are shown in Section 4.1.3.

4. Results

4.1. Standards

4.1.1. Sulfur four-isotope analysis (sessions 1 and 4)

Sulfur four-isotope analyses were performed in two separate sessions (#1 and 4). Session 1 (one day) confirmed the analysis conditions for sulfur four-isotope analysis and session 4 (four days in total) was for analysis of standards and pyrite samples. Results for standard pyrites (UWPy-1 and Ruttan pyrite) in both sessions are summarized in Table 2. Fig. 2 exhibits average $\delta^{34}S_{raw}$, $\Delta^{33}S_{raw}$ and $\Delta^{36}S_{raw}$ values of standard analyses (n = 4 to 10) according to the order of analysis time for each pyrite standard. The correction factors for instrumental biases of $\delta^{34}S$ (α_{SIMS}(pyrite)), $\Delta^{33}S$ (Bias ($\Delta^{33}S$)), and $\Delta^{36}S$ (Bias ($\Delta^{36}S$)) values of UWPy-1 were 1.0013 to 1.0033, 0.44 to 0.47‰, and −21.00 to −19.40‰, respectively. Those determined by Ruttan pyrite data (using $\delta^{34}S$ = 1.2‰, Crowe and Vaughan, 1996) were 1.0017 to 1.0024, 0.45 to 0.47‰, −20.76 to −19.41‰, respectively (Table 2). Note that the bias for $\Delta^{36}S$ was significantly different in these two sessions due to different tuning conditions. Thus, as observed in many studies, it is necessary to run appropriate standards in each analytical session (see, Kita et al., 2009; Valley and Kita, 2009). For these carefully prepared sample mounts, the sample exchange did not affect the raw values (Fig. 2), which was also found to be true for oxygen isotope analysis (Kita et al., 2009). However, as a precaution, a standard (UWPy-1) was mounted in the center of each mount and we recommend this procedure for similar studies.

The average value of spot-to-spot reproducibility (±2 Standard Deviation, 2 SD) of $\delta^{34}S$, $\Delta^{33}S$, and $\Delta^{36}S$ of eight bracketing analyses of UWPy-1 in the session 4 were ±0.23, ±0.05, and ±0.86‰, respectively (Table 2). The reproducibility of $\Delta^{33}S$ (±0.05) of this session is better than that of the former sulfur three-isotope analysis (±0.09; Williford et al., 2011) because a higher signal to noise ratio for the $^{33}S^{+}$ detection was achieved due to use of a higher intensity primary beam (~5 nA, ~20 μm in diameter) than that for the sulfur three-isotope analysis (~1.5 nA, ~10 μm in diameter).

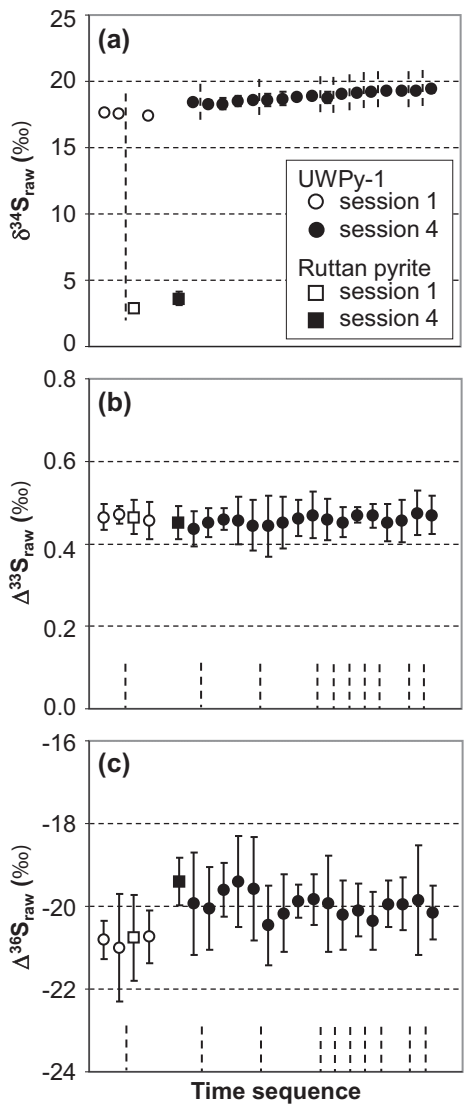

Fig. 2. Measured values of (a) $\delta^{34}S_{raw}$, (b) $\Delta^{33}S_{raw}$, and (c) $\Delta^{36}S_{raw}$ of UWPy-1 and Ruttan pyrite in sessions 1 and 4. Individual data points and errors are the averaged values of 4 to 10 analyses and their 2 SD, respectively. Measured values and the order of data starting from left are provided in Table 2. Intervening data for samples are omitted for clarity. The vertical dashed lines indicate sample changes.

4.1.2. Oxygen two-isotope test analysis (session 2)

Oxygen two-isotope ratios of the quartz standard UWQ-1 were measured with two different detector configurations (see Section 3.2.1 for the detector configurations). Four measurements of $\delta^{18}O$ were performed in each configuration and $\delta^{18}O_{raw}$ values (6.48 ± 0.32‰, 6.65 ± 0.18‰, n = 4, 2SD, for configurations #1 and #2, respectively) were consistent within analytical uncertainty (Table 3). These results indicate that the difference in relative sensitivity between H1 and H′2 FC detectors is ~0.5‰ at most.

4.1.3. Sulfur isotope analyses with the axial FC2 Faraday cup (session 3)

Results of sulfur isotope analyses (^{33}S, ^{34}S, and ^{36}S) with a single FC detector (the axial FC2) are summarized in Table 4. In this session, the $^{33}S^{-}$ signal is used as the denominator of the sulfur isotope ratios because the $^{32}S^{-}$ signal was not measured. The $\delta^{34/33}S_{raw}$ and $\delta^{36/33}S_{raw}$ are defined as deviations expressed by ‰ from VCDT values of $^{34}S/^{33}S$ and $^{36}S/^{33}S$ ratios (Ding et al., 2001, see also section S3 in Electronic Annex).

Average values of UWPy-1 were $\delta^{34/33}S_{raw}$ = 5.7 ± 1.1‰ and $\delta^{36/33}S_{raw}$ = −1.3 ± 5.0‰ (2SD, n = 8), respectively (Table 4). Reproducibility of sulfur isotope analyses with a single FC detector in this session was worse than that of sulfur isotope analyses with multiple FC detectors in sessions 1 and 4 because analysis with a single FC detector cannot compensate for either fluctuation or drift of secondary ion count rates during the analysis. Longer analysis time with a single

Table 3
The average $\delta^{18}O_{raw}$ values of UWQ-1 quartz standard with different analytical settings at WiscSIMS.

Configuration[a]	# of analysis	$\delta^{18}O_{raw}$[b]	2 SD
(1) L′2 + H1	4	6.48	±0.32
(2) L′2 + H′2	4	6.65	±0.18

[a] Configurations are described in the Section 3.2.1.
[b] $\delta^{18}O_{raw}$ is defined as $\{(^{18}O/^{16}O)_{measure}/0.0020052 - 1\} \times 1000$.

Table 4
Raw sulfur isotope ratios and count rates of baseline of UWPy-1 pyrite standard by the axial Faraday cup.

Analysis #	Sample	Sulfur isotope ratios						Count rates (cps)				
		$\delta^{34/33}S_{raw}$ [a]	2 SE [b]	$\delta^{36/33}S_{raw}$ [a]	2 SE [b]	$\Delta^{36/33}S_{raw}$ [c]	2 SE [b]	$^{33}S^-$	$^{34}S^-$	$^{36}S^-$	5 s after $^{34}S^-$ [d]	11 s after $^{34}S^-$ [e]
Isotope analysis												
#1	UWPy-1	4.39	±0.61	−4.7	±3.3	−17.3	±2.7	4.22E+07	2.38E+08	8.18E+05		
#2	UWPy-1	5.99	±0.77	−0.8	±3.6	−18.0	±2.8	4.03E+07	2.27E+08	7.84E+05		
#3	UWPy-1	5.79	±0.60	2.1	±4.5	−14.5	±3.4	4.05E+07	2.28E+08	7.90E+05		
#4	UWPy-1	5.94	±0.76	−2.7	±3.3	−19.7	±2.6	4.07E+07	2.29E+08	7.90E+05		
#5	UWPy-1	5.86	±0.73	1.0	±3.9	−15.8	±3.8	4.09E+07	2.30E+08	7.97E+05		
#6	UWPy-1	5.76	±0.93	0.5	±3.6	−16.1	±2.4	3.91E+07	2.20E+08	7.61E+05		
#7	UWPy-1	6.02	±0.76	−1.2	±3.0	−18.5	±2.2	3.93E+07	2.22E+08	7.65E+05		
#8	UWPy-1	5.74	±0.69	−4.3	±4.0	−20.8	±3.7	3.92E+07	2.21E+08	7.61E+05		
Average (±2 SD)		5.7	±1.1	−1.3	±5.0	−17.6	±4.2	4.03E+07	2.27E+08	7.83E+05		
Baseline count rate test												
#9	UWPy-1							4.61E+07	2.62E+08		2.46E+03	3.15E+02
#10	UWPy-1							4.59E+07	2.60E+08		1.44E+03	1.09E+03
#11	UWPy-1							4.37E+07	2.47E+08		1.66E+03	−8.81E+01
#12	UWPy-1							4.36E+07	2.47E+08		−1.42E+02	1.04E+03
#13	UWPy-1							4.25E+07	2.41E+08		1.44E+03	6.64E+02
#14	UWPy-1							4.06E+07	2.30E+08		5.03E+02	1.93E+03
Average (±2 SD)								4.37E+07	2.48E+08		1.2E+03	8E+02
								±4.2E+06	±2.4E+07		±1.8E+03	±1.4E+03

[a] The $\delta^{i/33}S_{raw}$ values (i = 34, 36) are defined as $\{(^iS/^{33}S)_{raw}/(^iS/^{33}S)_{VCTD} - 1\} \times 1000$.
[b] 2 SE of measured ratios of 20 cycles in each analysis.
[c] Due to significant drift of measured $\delta^{34/33}S_{raw}$ and $\delta^{36/33}S_{raw}$ values within each analysis, the $\Delta^{36/33}S_{raw}$ value of each analysis is determined as the average $\Delta^{36/33}S_{raw}$ value of individual 20 cycles using the formula (xi) in section S3 in Electronic Annex.
[d] FC baseline count rate at 5 s after measurements of $^{34}S^-$.
[e] FC baseline count rate at 11 s after measurements of $^{34}S^-$.

FC detector than that with multiple FC detectors (400 s vs. 180 s) can increase the influence of variation of secondary ion count rates. Because systematic changes in $\delta^{34/33}S_{raw}$ values in this session, which consistently decreased by approximately 4‰, were recognized within single analyses (Fig. S2b in Electronic Annex), deviation of $^{36}S/^{33}S$ ratio from the mass-dependent fractionation ($\Delta^{36/33}S$, defined by formula (xi) in section S3 in Electronic Annex) was calculated using $\delta^{34/33}S_{raw}$ and $\delta^{36/33}S_{raw}$ values for each cycle and the average $\Delta^{36/33}S$ value of all cycles was reported as the result of a single analysis. The average $\Delta^{36/33}S$ value of eight UWPy-1 analyses was −17.6 ± 4.2‰ (2 SD, Table 4).

The results of the baseline count-rate measurements of the axial FC2 FC detector are also shown in Table 4. The baseline count rates of the axial FC2 detector at 5 s after the detection of the $^{34}S^-$ signal tend to show positive values (five out of six measurements show positive values, average = (1.2 ± 1.8) × 10^3 cps, 2 SD), suggesting measured current by the FC amplifier was slightly higher than the intensity of normal dark current. Since the baseline count rates at 11 s after the detection of the $^{34}S^-$ signal also tend to show positive values (five out of six measurements, average = (0.8 ± 1.4) × 10^3 cps, 2 SD). In session 3, the $^{36}S^-$ signal was measured at 5 s after detection of $^{34}S^-$ signal. Results of the baseline count-rate measurements suggest that the baseline count rate of the axial FC2 detector could have been higher than normal by ~1000 cps when the $^{36}S^-$ signal was measured. Although an increase of the baseline count rate of ~1000 cps was negligible for $^{33}S^-$ (~4.0 × 10^7 cps) and $^{34}S^-$ (~2.3 × 10^8 cps), this would cause a positive offset by 1 to 2‰ for $^{36}S^-$ (~7.8 × 10^5 cps). True $\delta^{36/33}S_{raw}$ and $\Delta^{36/33}S$ values could be 1 to 2‰ lower than the measured value, resulting in values that are about 19‰ lower than the expected $\delta^{36/33}S_{raw}$ and $\Delta^{36/33}S$ values.

In summary, sulfur isotope analyses (^{33}S, ^{34}S, and ^{36}S) with a single FC detector were performed and the measured $^{36}S/^{33}S$ ratio by the single FC detector was about 19‰ lower than the expected value (−19 ± 4‰) given an offset of the baseline count rate of the axial FC2 detector. As we described in Section 4.1.1, the measured $^{36}S/^{32}S$ ratio by multiple FC detectors in sessions 1 and 4 was also lower than the expected value by about 20‰. Large apparent instrumental biases for ^{36}S measurement of approximately −19‰ were consistently observed by measurements with both a single FC detector and multiple-FC detectors.

4.2. Detrital Archean pyrite grains in ~2.4 Ga glaciogenic sandstone (session 4)

Sulfur isotope ratios of 25 detrital pyrite grains from glaciogenic sandstone (MB190583) of the ~2.4 Ga Meteorite Bore Member of the Turee Group were measured in session 4. As we described in Section 4.1.1, the calculated $\Delta^{36}S_{raw}$ values of the UWPy-1 standard normalized to the $^{36}S/^{32}S$ ratio in Ding et al. (2001) consistently exhibit offset by approximately −20‰ (Table 2) for the simultaneous sulfur four-isotope analyses with multiple Faraday cups. This 20‰ offset in $^{36}S/^{32}S$ will be discussed below. Regardless of the reason, it does not cause systematic error in comparing values of ^{36}S relative to the UWPy-1 standard ($\Delta^{36}S = -0.21 \pm 0.24$‰, Table 1) (see Section 5.1.4). Sulfur isotope ratios of $\delta^{34}S$, $\Delta^{33}S$, and $\Delta^{36}S$, of detrital pyrite grains are summarized in Table 5, after correction for instrumental biases. Uncertainties of sulfur isotope ratios of samples are from 2 SD of bracketing standard pyrite analyses and uncertainty of sulfur isotope ratios of UWPy-1 (Table 1). Since sulfur three-isotope ratios of 23 out of 25 pyrite grains were reported in Williford et al. (2011), previous data were also listed in Table 5 for comparison.

Most pyrite grains have positive values in $\delta^{34}S$ (up to 13.5‰ VCDT) and $\Delta^{33}S$ (up to 11.66‰) (Fig. 3a). One rounded pyrite grain (g30, Fig. 1c) was analyzed twice and has distinct and heterogeneous sulfur isotope ratios ($\delta^{34}S = -32.7$‰ and −27.4‰, $\Delta^{33}S = -2.74$‰ and −3.03‰, respectively, Fig. 3a, Table 5). Many pyrite grains have a significant anomaly in $\Delta^{36}S$, and the $\Delta^{33}S$ and $\Delta^{36}S$ values of each pyrite grain are distributed along a linear trend (Fig. 3b). The g30 pyrite grain has the highest $\Delta^{36}S$ value ($\Delta^{36}S$ ~ 4.6‰) among detrital pyrite grains in this study.

The $\Delta^{33}S$ and $\Delta^{36}S$ values of the pyrite aggregate (g9, Fig. 1f) deviate from the linear trend of other pyrite grains (Fig. 3b). The calculated regression line of the $\Delta^{33}S - \Delta^{36}S$ linear trend, excluding data of the pyrite aggregate g9, is $\Delta^{36}S = (-0.96 \pm 0.10) \times \Delta^{33}S + (0.72 \pm 0.38)$

Table 5
Sulfur four-isotope ratios of detrital pyrites in glaciogenic sandstone (190583) measured at WiscSIMS.

Grain, analysis #	Shape	This study												Williford et al. (2011)			
		$\delta^{34}S$ (‰ VCDT)	2 SD	$\delta^{33}S$[a] (‰ VCDT)	2 SD	$\delta^{36}S$[a] (‰ VCDT)	2 SD	$\Delta^{33}S$ (‰)	2 SD	$\Delta^{36}S$ (‰)	2 SD	$^{32}SH^-$ tail[b] (‰)	$^{32}S^-$ yield (10^9 cps/nA)	$\delta^{34}S$[c] (‰ VCDT)	2 SD	$\Delta^{33}S$ (‰)	2 SD
g1, #24	Rounded	**13.30**	**±0.33**	**16.96**	**±0.17**	**16.67**	**±1.21**	**10.13**	**±0.03**	**−8.74**	**±1.04**	0.0014	1.08	**13.82**	**±0.26**	**10.17**	**±0.10**
, #68[d]		**13.46**	**±0.25**	**17.13**	**±0.14**	**16.00**	**±1.36**	**10.22**	**±0.06**	**−9.73**	**±1.27**	0.0016	0.94	**13.16**	**±0.26**	**10.00**	**±0.10**
g1 average		13.39	±0.20	17.03	±0.11	16.46	±0.89	10.15	±0.03	−9.13	±0.80						
g2, #25	Rounded	**3.67**	**±0.33**	**2.41**	**±0.17**	**6.85**	**±1.21**	**0.53**	**±0.03**	**−0.12**	**±1.04**	0.0074	1.07	**3.68**	**±0.26**	**0.46**	**±0.10**
g3, #26	Anhedral[f]	**2.58**	**±0.33**	**2.68**	**±0.17**	**3.75**	**±1.21**	**1.35**	**±0.03**	**−1.16**	**±1.04**	0.0062	1.08	**2.53**	**±0.26**	**1.40**	**±0.10**
g4, #27	Rounded	**5.76**	**±0.33**	**6.07**	**±0.17**	**8.93**	**±1.21**	**3.11**	**±0.03**	**−2.04**	**±1.04**	0.0015	1.07	**5.74**	**±0.26**	**3.11**	**±0.10**
g7, #28	Rounded	**1.60**	**±0.33**	**1.70**	**±0.17**	**3.22**	**±1.21**	**0.88**	**±0.03**	**0.17**	**±1.04**	0.0010	1.07	**2.11**	**±0.23**	**0.91**	**±0.12**
g8, #33	Rounded	**11.38**	**±0.45**	**7.51**	**±0.23**	**20.63**	**±1.11**	**1.66**	**±0.03**	**−1.10**	**±0.68**	0.0011	1.08	**11.10**	**±0.23**	**1.69**	**±0.12**
g9, #35	Aggregate	**4.77**	**±0.45**	**3.07**	**±0.23**	**6.85**	**±1.10**	**0.61**	**±0.03**	**−2.23**	**±0.68**	0.0092	1.06	–	–	–	–
, #57		**4.36**	**±0.25**	**2.80**	**±0.14**	**6.12**	**±1.36**	**0.55**	**±0.06**	**−2.19**	**±1.27**	0.0092	1.02	–	–	–	–
g9 average		4.48	±0.22	2.91	±0.12	6.31	±0.73	0.60	±0.02	−2.22	±0.60						
g10, #36[e]	Anhedral[f]	**−0.41**	**±0.45**	**0.63**	**±0.23**	**−0.83**	**±1.10**	**0.84**	**±0.03**	**−0.05**	**±0.68**	0.0022	0.99	**−1.57**	**±0.23**	**0.47**	**±0.12**
g13, #37	Subhedral[f]	**2.48**	**±0.45**	**2.26**	**±0.23**	**6.02**	**±1.10**	**0.98**	**±0.03**	**1.31**	**±0.68**	0.0016	1.06	**2.71**	**±0.23**	**0.97**	**±0.12**
, #38		**2.74**	**±0.45**	**2.42**	**±0.23**	**5.47**	**±1.10**	**1.01**	**±0.03**	**0.26**	**±0.68**	0.0012	1.06	**2.85**	**±0.23**	**1.04**	**±0.12**
g13 average		2.61	±0.32	2.34	±0.17	5.75	±0.78	1.00	±0.02	0.78	±0.48						
g14, #39	Rounded[f]	**1.06**	**±0.45**	**0.59**	**±0.23**	**2.69**	**±1.10**	**0.04**	**±0.03**	**0.68**	**±0.68**	0.0014	1.02	**2.00**	**±0.14**	**0.15**	**±0.12**
g18, #44	Subhedral	**6.41**	**±0.43**	**3.32**	**±0.23**	**12.38**	**±1.40**	**0.03**	**±0.06**	**0.17**	**±1.13**	0.0061	1.08	**6.19**	**±0.14**	**0.05**	**±0.12**
g20, #45	Rounded	**1.76**	**±0.43**	**2.39**	**±0.23**	**2.65**	**±1.40**	**1.48**	**±0.06**	**−0.70**	**±1.13**	0.0023	1.06	**1.48**	**±0.14**	**1.53**	**±0.12**
g21, $46	Rounded	**2.24**	**±0.43**	**2.02**	**±0.23**	**3.42**	**±1.40**	**0.87**	**±0.06**	**−0.84**	**±1.13**	0.0009	1.07	**2.12**	**±0.14**	**0.80**	**±0.12**
g24, #47	Anhedral	**2.79**	**±0.43**	**5.94**	**±0.23**	**1.12**	**±1.40**	**4.50**	**±0.06**	**−4.18**	**±1.13**	0.0011	1.05	**3.29**	**±0.17**	**4.36**	**±0.09**
g29, #48	Rounded[f]	**0.16**	**±0.43**	**0.08**	**±0.23**	**1.34**	**±1.39**	**0.00**	**±0.06**	**1.04**	**±1.13**	0.0017	1.06	**0.07**	**±0.17**	**−0.05**	**±0.09**
, #49		**0.15**	**±0.43**	**0.03**	**±0.23**	**1.49**	**±1.39**	**−0.05**	**±0.06**	**1.20**	**±1.13**	0.0012	1.06	–	–	–	–
g29 average		0.15	±0.30	0.05	±0.16	1.41	±0.99	−0.03	±0.04	1.12	±0.80						
g30, #50	Rounded	**−32.72**	**±0.43**	**−19.72**	**±0.23**	**−56.65**	**±1.38**	**−2.74**	**±0.06**	**4.59**	**±1.13**	0.0060	1.06	**−31.97**	**±0.17**	**−2.45**	**±0.09**
, #51		**−27.40**	**±0.43**	**−17.24**	**±0.23**	**−46.82**	**±1.38**	**−3.03**	**±0.06**	**4.61**	**±1.13**	0.0067	1.05	**−28.09**	**±0.17**	**−3.57**	**±0.09**
g30 average		−30.06	±3.76	−18.48	±1.75	−51.74	±6.99	−2.89	±0.21	4.60	±0.80						
g31, #52	Anhedral	**2.96**	**±0.43**	**3.54**	**±0.23**	**4.46**	**±1.40**	**2.01**	**±0.06**	**−1.17**	**±1.13**	0.0011	1.07	**3.00**	**±0.14**	**2.09**	**±0.10**
g44, #66	Rounded	**−6.23**	**±0.25**	**−2.15**	**±0.14**	**−10.68**	**±1.36**	**1.06**	**±0.06**	**1.11**	**±1.27**	0.0019	1.09	**0.93**	**±0.14**	**1.00**	**±0.10**
g45, #58	Rounded	**4.64**	**±0.25**	**6.98**	**±0.14**	**4.59**	**±1.36**	**4.60**	**±0.06**	**−4.24**	**±1.27**	0.0010	1.10	**4.56**	**±0.24**	**4.62**	**±0.09**
, #59		**4.96**	**±0.25**	**7.21**	**±0.14**	**5.72**	**±1.36**	**4.66**	**±0.06**	**−3.73**	**±1.27**	0.0010	1.09	**4.98**	**±0.14**	**4.53**	**±0.10**
g45 average		4.80	±0.18	7.10	±0.10	5.16	±0.96	4.63	±0.04	−3.98	±0.90						
g46, #60	Anhedral[f]	**12.96**	**±0.25**	**18.31**	**±0.14**	**16.01**	**±1.36**	**11.66**	**±0.06**	**−8.75**	**±1.27**	0.0016	1.07	**12.71**	**±0.24**	**11.73**	**±0.09**
g48, #61	Anhedral	**2.48**	**±0.25**	**3.66**	**±0.14**	**3.04**	**±1.36**	**2.38**	**±0.06**	**−1.68**	**±1.27**	0.0062	1.09	**2.75**	**±0.24**	**2.37**	**±0.09**
g50, #65	Anhedral[f]	**3.74**	**±0.25**	**2.99**	**±0.14**	**6.35**	**±1.36**	**1.06**	**±0.06**	**−0.78**	**±1.27**	0.0028	1.08	**4.20**	**±0.24**	**1.00**	**±0.09**
g53, #64	Rounded	**0.89**	**±0.25**	**0.56**	**±0.14**	**1.47**	**±1.36**	**0.10**	**±0.06**	**−0.22**	**±1.27**	0.0011	1.09	**0.77**	**±0.19**	**0.06**	**±0.08**
g54, #62	Rounded[f]	**4.81**	**±0.25**	**8.04**	**±0.14**	**3.54**	**±1.36**	**5.56**	**±0.06**	**−5.63**	**±1.27**	0.0041	1.05	**4.99**	**±0.19**	**5.39**	**±0.08**
, #63		**4.73**	**±0.25**	**8.15**	**±0.14**	**3.18**	**±1.36**	**5.71**	**±0.06**	**−5.83**	**±1.27**	0.0049	1.02	–	–	–	–
g54 average		4.77	±0.18	8.09	±0.10	3.36	±0.96	5.64	±0.04	−5.73	±0.90						
g58, #67	Rounded	**3.90**	**±0.25**	**5.50**	**±0.14**	**4.41**	**±1.36**	**3.49**	**±0.06**	**−3.01**	**±1.27**	0.0011	1.09	–	–	–	–

[a] Values are calculated based on measured $\delta^{34}S_{VCDT}$, $\Delta^{33}S$, $\Delta^{36}S$ values and equations of mass-dependent sulfur isotope fractionation.
[b] Amounts of correction (in ‰) of the interference $^{32}SH^-$ signal to the $^{33}S^-$signal.
[c] Data are recalculated using new sulfur isotope ratios of UWPy-1.
[d] The analysis partially miss pyrite grain (~80% pyrite and ~20% silicates).
[e] The analysis pit contains many quartz inclusions.
[f] Pyrite contains many silicate inclusions.

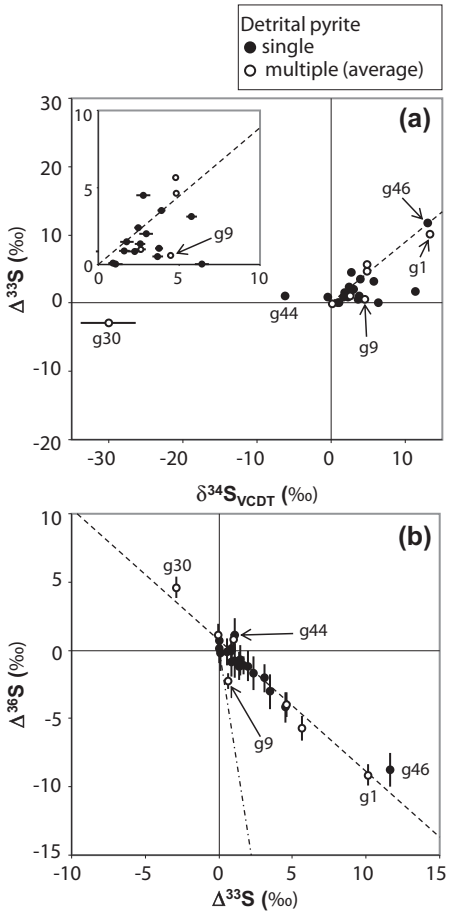

Fig. 3. Sulfur isotope compositions of detrital pyrite grains in the glaciogenic sandstone, MB190583, from the 2.4 Ga Meteorite Bore Member of the Turee Creek Group. (a) $\delta^{34}S$ vs. $\Delta^{33}S$, and (b) $\Delta^{33}S$ vs. $\Delta^{36}S$ of individual pyrite grains (filled symbol = single analysis data, open symbol = averaged values of multiple analyses, Table 5). Pyrite grain names that have distinct sulfur isotope ratios are shown. The dashed line in (a) indicates the slope = −0.89 Archean reference array (Ono et al., 2009b). The dashed line in (b) is the regression line ($\Delta^{36}S = -0.96 \times \Delta^{33}S + 0.72$) of detrital pyrite grain data (excluding g9). The dashed-dotted line in (b) indicates the slope = −6.85 line observed in sedimentary sulfides of Phanerozoic age (Ono et al., 2006b).

[MSWD = 2.4, errors are 95% confidence, see also Fig. S3 in Electronic Annex].

5. Discussion

5.1. Evaluation of in situ sulfur four-isotope analysis of pyrite

5.1.1. Reproducibility of $\delta^{34}S$, $\Delta^{33}S$, and $\Delta^{36}S$ values of bracketing standard analyses

Values of two standard deviation (2 SD) of bracketing standard analyses ($n \geq 8$) are ±0.05 to ±0.52‰ (average = ±0.23‰) for $\delta^{34}S$, ±0.02 to ±0.07‰ (average = ±0.05‰) for $\Delta^{33}S$, and ±0.41 to ±1.33‰ (average = ±0.86‰) for $\Delta^{36}S$ (Table 2). The reproducibility of the $\Delta^{36}S$ value is comparable with those of previous studies using an EM detector for the ^{36}S measurement: 0.42 to 1.34‰ (2 SD, Whitehouse, 2013), ca. 1.0‰ (2 SD, Roerdink et al., 2013), and 0.5‰ (2 SD, Farquhar et al., 2013). We used a higher intensity beam (4.5 to 5.3 nA in this study vs. 2.5 to 4 nA in previous studies) and a FC detector for measurement of ^{36}S. Use of a FC detector is advantageous because the sensitivity of a FC detector is stable and no detectable drift of sensitivity occurs within a single analysis, but such drift is common with an EM, especially at higher count rates. In addition, as shown in Section 4.1.2, the difference in relative sensitivity among multiple FC detectors is very small (e.g. less than 0.5‰ between H1 and H′2 FC detectors). For these reasons, we could reduce process of data reduction and uncertainty and the results by FC detector for ^{36}S are more accurate than if using an EM detector. Changes of FC amplifier design (e.g., ±0.41‰, 2 SD, Ireland et al., 2014) may lead to further improvements in accuracy and precision for in situ sulfur four-isotope analysis.

Higher precision measurements of $\Delta^{33}S$ are another benefit to using multiple FC detectors because of higher count rate of $^{33}S^-$ relative to that of analysis with an EM detector for measurement of ^{36}S. The average reproducibility of $\Delta^{33}S$ (±0.05‰, 2 SD) in this study is better than those of previous studies (±0.22‰ for Whitehouse, 2013, ±0.4‰ for Roerdink et al., 2013, ±0.08‰ for Farquhar et al., 2013, and ±0.46‰ for Ireland et al., 2014). Improved reproducibility of $\delta^{34}S$ value is possible through careful tuning of the primary beam conditions. This will be discussed in the following section.

5.1.2. Significance of the primary beam condition for sulfur isotope analysis

Instrumental bias varied according to different analytical conditions used in this study by up to 1‰. For example, the $\delta^{34}S_{raw}$ values of both UWPy-1 and Ruttan pyrite of session 4 were consistently higher by ~1‰ than those of session 1 (Fig. 2a). In addition, the $\delta^{34}S_{raw}$ values of UWPy-1 systematically increased by ~1‰ throughout session 4, leading to drift in the correction factor of the instrumental bias for $\delta^{34}S$ value (α_{SIMS}(pyrite)) (Fig. 2a, Table 2). It is unlikely that this drift was caused by change of either baseline or efficiency of FC detectors because no significant drift was observed for the $\Delta^{33}S$ and $\Delta^{36}S$ values (Fig. 2b and c), which can be more sensitive to detector's condition than the $\delta^{34}S$ value because count rates of $^{33}S^-$ and $^{36}S^-$ signals are lower than those of $^{32}S^-$ and $^{34}S^-$. The observed drift is apparently mass-dependent and is probably the result of changing instrumental mass-dependent fractionation caused by gradual increase of primary beam size during the session.

Fig. 4a and b shows analysis pit shapes at the beginning and the end of session 4. It is evident that the primary beam aperture which adjusts the primary beam shape was worn away by sputtering of 10-kV-accelerated Cs^+ ion beam and the primary beam size was getting larger throughout analysis session. Since the primary beam intensity was set at ~5 nA, the analysis pit depth would become shallower as the pit size became larger toward the end of analysis session. This subtle change of primary beam condition probably affects the instrumental bias for $\delta^{34}S$ value, α_{SIMS}(pyrite), because the magnitude of drift of $\delta^{34}S_{raw}$ for each cycle within a single analysis became smaller toward the end of session 4 (Fig. 4c), resulting in the internal error (2SE) of the $\delta^{34}S_{raw}$ values of 20 cycles within each analysis becoming smaller (e.g., ±0.23‰ for analysis #23 and ±0.03 for analysis #268, respectively, Table S4 in Electronic Annex). Diminishing the change of $\delta^{34}S_{raw}$ within each analysis is consistent with the increase of $\delta^{34}S_{raw}$ of each analysis, which corresponds to increase of α_{SIMS}(pyrite). In addition, significant increase of the sulfur ion yield was observed after a certain period of time (e.g., Fig. S2a in Electronic Annex). Because the timing of increase of the sulfur ion yield became earlier when a smaller beam with the same intensity (resulting deeper analysis pits) was applied, the sulfur ion yield seems to be also sensitive to the analysis pit depth. A slightly defocused primary beam (~20 μm in diameter) was applied instead of a well-focused primary beam (~15 μm in diameter) for all sulfur four-isotope analysis sessions to accomplish each analysis before a significant increase of the sulfur ion yield (Fig. S2a in Electronic Annex).

Because the drift of instrumental bias for $\delta^{34}S$ was gradual and because the internal error of each analysis is comparable to the reproducibility of spot-to-spot analyses, frequent measurements of UWPy-1 (e.g., bracketing analyses after 10 to 20 sample analyses) are enough to represent uncertainty of sample analysis. However, if primary beam conditions changed more rapidly, then a much larger internal error could occur due to larger drift and it would be difficult to achieve sub-permil precision and accuracy of $\delta^{34}S$ values. A slightly defocused

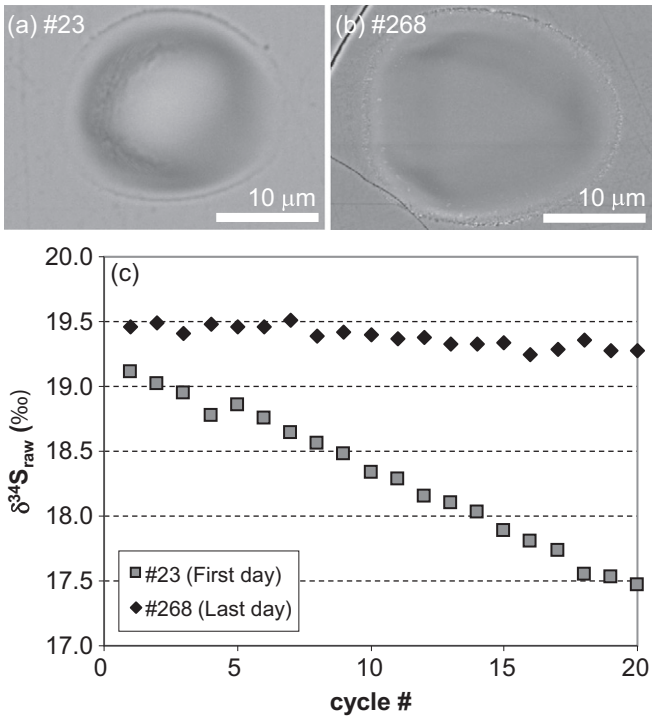

Fig. 4. Examples of analysis pit shape and measured sulfur isotope ratios. BSE images of an analysis pit of (a) the first day (analysis #23) and (b) an analysis pit of the fourth day of session 4 (analysis #268). The primary beam formed flat-bottom pits. The outermost ring structures of analysis pits were formed by aberration of primary beam. (c) Comparison of temporal change of measured $\delta^{34}S_{raw}$ values of individual cycles of the analyses #23 and #268 in session 4. Temporal change in $^{34}S^-$ count rate is shown in Fig. S2a in Electronic Annex.

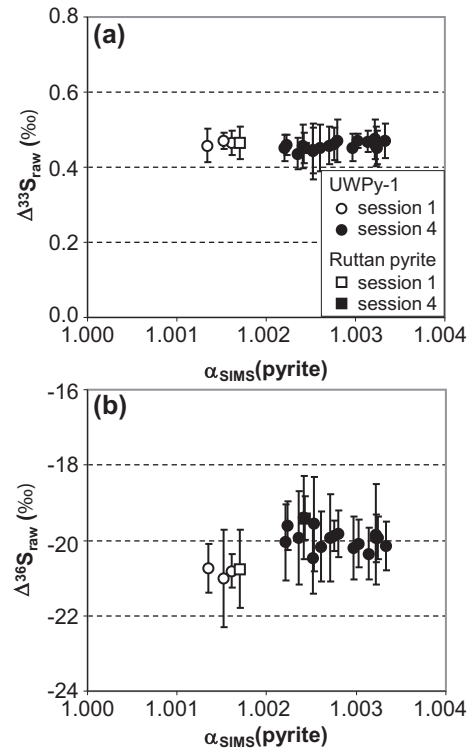

Fig. 5. Comparisons of instrumental bias between UWPy-1 and Ruttan pyrites: (a) $\Delta^{33}S_{raw}$ and α_{SIMS}(pyrite) and (b) $\Delta^{36}S_{raw}$ and α_{SIMS}(pyrite).

primary beam condition that diminishes changes of $\delta^{34}S_{raw}$ and the sulfur ion yield is an important factor to achieve high precision and accuracy of sulfur four-isotope analysis.

5.1.3. Consistency of correction factors of $\delta^{34}S$, $\Delta^{33}S$, and $\Delta^{36}S$ for pyrite standards

The instrumental bias for $\delta^{34}S$ values (α_{SIMS}(pyrite)) determined by analyses of UWPy-1 ($\delta^{34}S = 16.04 \pm 0.18$‰ VCDT, Table 1) and Ruttan pyrite ($\delta^{34}S = 1.2 \pm 0.1$‰ VCDT, Crowe and Vaughan, 1996) were consistent within analytical uncertainty (e.g., α_{SIMS}(pyrite) =1.0024 ± 0.0001 for UWPy-1 analyses #5–9 and #13–16, and 1.0024 ± 0.0004 for Ruttan pyrite analyses #10–13 in session 4, respectively, Table 2). Since Ruttan pyrite grains in this study were separated from the same sample that was used in Crowe (1990), it is appropriate that they have the same sulfur isotope composition as reported by Crowe and Vaughan (1996). Contrary to the $\delta^{34}S_{raw}$ values, all the $\Delta^{33}S_{raw}$ values of both UWPy-1 and Ruttan pyrite were constant within analytical uncertainty through the analysis sessions (Fig. 2b). There was no significant correlation between the α_{SIMS}(pyrite) values and the $\Delta^{33}S_{raw}$ values for each session (Fig. 5a). These data indicate the following: 1) the same correction factor, Bias($\Delta^{33}S$), can be applied to determine mass independent isotope anomalies in ^{33}S ($\Delta^{33}S$) for pyrites that have different $\delta^{34}S$ values, and 2) the correction factor, Bias($\Delta^{33}S$), is independent of changes of the instrumental bias, α_{SIMS}(pyrite). The consistency of the correction factors, Bias($\Delta^{33}S$), of UWPy-1 and Ruttan pyrite indicates that the same correction factor determined by running standard UWPy-1 can be applied to estimate the $\Delta^{33}S$ values of samples with variable $\delta^{34}S$. The $\Delta^{36}S_{raw}$ values of both UWPy-1 and Ruttan pyrite are also constant within analytical uncertainty for each session (Fig. 2c). As is the case in the $\Delta^{33}S_{raw}$ values, no significant correlation was observed between the α_{SIMS}(pyrite) values and the $\Delta^{36}S_{raw}$ values for each session (Fig. 5b). These results indicate that the correction factors of running standard UWPy-1 (α_{SIMS}(pyrite) for $\delta^{34}S$, Bias($\Delta^{33}S$) for $\Delta^{33}S$, and Bias($\Delta^{36}S$) for $\Delta^{36}S$) can be applied to estimate sulfur isotope ratios of samples with variable $\delta^{34}S$.

The average $\Delta^{36}S_{raw}$ values of the sessions 1 and 4 are different by ~1‰ (Fig. 2c). This difference could result from the differences in the baseline calibration of the FC amplifiers. The baseline of the FC amplifiers was measured for 64 s at the beginning of each session. Because a typical count rate of $^{36}S^-$ is ~8×10^5 cps, uncertainty of the baseline calibration of about ±500 cps could cause a systematic bias of ~1‰ for the $\Delta^{36}S_{raw}$ values for every session. However, the consistent $\Delta^{36}S_{raw}$ values of standard pyrites are within 2SD of the bracketing analyses for each session indicating that accurate values can be obtained if analyses of the standard are performed frequently with the same analytical condition for the unknown sample analyses.

5.1.4. $^{36}S/^{32}S$ ratio of VCDT deduced from ion microprobe analysis

A $\Delta^{36}S_{raw}$ value of approximately −20‰ (Table 2) was consistently obtained for the simultaneous sulfur four-isotope analysis of UWPy-1 in sessions 1 and 4. This indicates that the measured $^{36}S/^{32}S$ values are lower by approximately 20‰ than the $^{36}S/^{32}S$ value derived using the VCDT value of Ding et al. (2001) (1/6515). The sample-standard normalization of the gas source mass spectrometry methods does not require an absolute $^{36}S/^{32}S$ value for VCDT in order to determine $\Delta^{36}S$.

There are several possible causes of the observed −20‰ offset in the $\Delta^{36}S_{raw}$ value by SIMS analysis: (1) the relative efficiency of the FC detector at H′2 position which detected the $^{36}S^-$ signal was lower than others by approximately 20‰; (2) scattered ions systematically hit the flight tube of the mass spectrometer at mass higher than 36 amu causing an unexpected shift of the H′2 FC baseline; (3) part of the $^{36}S^-$ signal was irregularly blocked by an obstacle in the flight tube or detectors after the electromagnet analyzer due to its outermost trajectory among the measured signals; or (4) the $^{36}S/^{32}S$ ratio of VCDT

is smaller by approximately 20‰ than the VCDT value estimated by Ding et al. (2001) used to calculate $\delta^{36}S_{raw}$ and $\Delta^{36}S_{raw}$ values.

Hypotheses (1), (2), and (3) are unlikely because a deficit of ^{36}S of approximately 19‰ was consistently observed by analyses with the axial FC2 detector (session 3). In session 3, all three sulfur ions ($^{33}S^-$, $^{34}S^-$, and $^{36}S^-$) were detected by the same detector located at the axial position of the mass spectrometer, so that neither a change of relative sensitivity for individual ion detections (hypothesis 1) nor any effects by interference signals or irregular loss by an obstacle in the secondary ion path (hypotheses 2 and 3) are expected. In addition, results of the oxygen two-isotope test analyses (session 2) described in Section 4.1.2 indicate that the differences in relative sensitivity between H1 detector and H′2 detector is ~0.5‰ at most. Thus, hypotheses (1), (2), and (3) have been evaluated and cannot account for the large difference in measured ^{36}S. Although the uncertainty of results of session 3 (~4‰, 2 SD) is larger than those of sessions 1 and 4 (~0.9‰, 2 SD) due to a temporal variation of the secondary ion intensities during the analysis with a magnet peak switching mode (Table 4, see also Section 4.1.3), we adopt −19 ± 4‰ for the discussion of ^{36}S abundance because we cannot tell the true instrumental bias for ^{36}S by analyses with multiple Faraday cups.

In contrast to hypotheses (1), (2), and (3), hypothesis (4) proposes that the SIMS data are correct and that the true VCDT $^{36}S/^{32}S$ ratio is lower by approximately 19‰ (i.e., 1/6641 vs. 1/6515), explaining the consistently lower $^{36}S^-$ signal for all of the different analytical settings. This discrepancy is significantly larger than the reported uncertainty for analysis of SF_6 in a single-detector gas-source mass spectrometer ($^{36}S/^{32}S = 1 / (6515 \pm 20)$, ~3‰ in $\delta^{36}S$, Ding et al., 2001). However, unlike the measurements of ^{32}S, ^{33}S, and ^{34}S abundances of the IAEA reference materials (IAEA-S-1, IAEA-S-2, and IAEA-S-3), the measurement of ^{36}S abundance of IAEA-S-1 was not calibrated by analyses of synthetically enriched sulfur-isotope materials because of lack of ^{36}S-enriched starting material. If the conversion factor (defined as $[f(^{32}S) / f(^{i}S)] / [I(^{32}S) / I(^{i}S)]$, f = abundance of sulfur isotope, I = measured current for each sulfur isotope by the detector of the instrument, i = 33, 34, and 36; Ding et al., 2001) correlates with either mass difference or ratio of measured currents, the conversion factor for $^{32}S/^{36}S$ could be different from those for $^{32}S/^{33}S$ and for $^{32}S/^{34}S$. Ding et al. (2001) reported the estimated ^{36}S abundance relative to ^{32}S for VCDT as a "calculated value", which was treated separately from the ^{33}S and ^{34}S abundances relative to ^{32}S. Our data show that the ^{36}S abundance of VCDT is approximately 19‰ less than the reported abundance. Further absolute abundance analyses are required to refine the value for ^{36}S abundance of VCDT.

5.1.5. Meteorite bore samples

Fig. 6 exhibits comparisons of $\delta^{34}S$ and $\Delta^{33}S$ values measured by SIMS in this study and Williford et al. (2011). Because shapes of most pyrite grains did not change after repolishing of the sample mount, we could measure sulfur isotope ratios of similar domains where Williford et al. (2011) measured. Although the primary beam currents of this study are stronger and the spot sizes are larger (5 nA, 20 μm in diameter) than that of Williford et al. (2011) (1.5 nA, 10 μm in diameter), more than 70% of data (19/27 for $\delta^{34}S$ and 20/27 for $\Delta^{33}S$) are consistent within analytical uncertainties (2SD) and most data are tightly distributed along the 1 to 1 line (Fig. 6). This indicates (1) the $\delta^{34}S$ and $\Delta^{33}S$ analysis of pyrite sample by SIMS is reproducible even though different primary beam conditions and different detector settings (sulfur three-isotope vs. sulfur four-isotope) were used in separate sessions, and (2) SIMS has capability to measure sulfur isotope ratios of the same domains of individual pyrite grains as far as the same domain remains after repolishing and removal of previous analysis pits.

There are several pyrite grains whose data deviate from the 1 to 1 line especially for the $\delta^{34}S$ values. Two analyses of the g30 pyrite grain indicate that some detrital pyrite grains have highly heterogeneous sulfur isotope ratios. This is consistent with results of previous sulfur

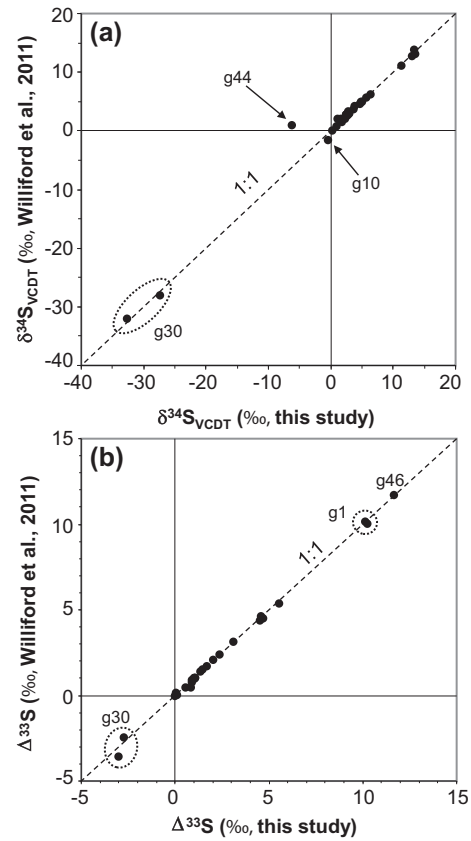

Fig. 6. Comparisons of (a) $\delta^{34}S$ and (b) $\Delta^{33}S$ values of individual pyrite grains from this study and Williford et al. (2011). The dashed lines indicate the 1:1 relation between this study and Williford et al. (2011). Precision (2 SD) for individual analyses is smaller than symbols.

3-isotope analyses of the same grain that vary by up to 9.4‰ (see the image s190583 g30 in Fig. S6 in the Electronic Annex of Williford et al., 2011). For g44 and g10 whose data deviated from the 1 to 1 line, the sulfur isotope analysis points in this session are different from where previously measured by Williford et al. (2011) because of changes of the sample surface after grinding and removal of previous SIMS analysis pits (Fig. S1 in Electronic Annex). It is likely that significant deviation of sulfur isotope data between two separate sessions (e.g., g10, g30, and g44 in Fig. 6) represent intra-grain sulfur isotope heterogeneity of detrital pyrite grains.

5.2. Applications for Archean sulfur isotope systematics

The measurement of ^{36}S in addition to sulfur three-isotopes (^{32}S, ^{33}S, and ^{34}S) provides an additional constraint for better understanding the sulfur isotope geochemistry of the near-surface environment of Earth in the Precambrian. The origins of pyrite grains in the glaciogenic sandstone (MB190583) may relate to atmospheric, oceanic, and biogenic conditions at the time of the GOE. As previously discussed by Williford et al. (2011), the wide range of $\Delta^{33}S$ values (−3.03 to 11.66‰, Fig. 6b, Table 5) of pyrite grains is distinct from that of authigenic pyrite grains throughout the section of the same outcrop ($\Delta^{33}S$ = −0.8 to 1.0‰; Williford et al., 2011), indicating that these pyrite grains formed before deposition of the glacial sediment and were potentially derived from multiple sources of various ages. Many data are distributed along a line with slope = 0.89 in the $\delta^{34}S$–$\Delta^{33}S$ plot (Fig. 3a) likely indicating that a major source of sulfur was atmospherically influenced elemental sulfur (S_8) (Farquhar and

Wing, 2003; Ono et al., 2003). Some pyrite data deviate from a line with slope = 0.89 and are distributed between the line with slope = 0.89 and the x-axis. These data likely result from mixing with elemental sulfur and ^{34}S-enriched seawater sulfate (e.g., Ono et al., 2003; Kamber and Whitehouse, 2007). Negatively fractionated δ^{34}S values (−6 to −30‰) are observed in pyrite grains g30 and g44, and likely record microbial sulfate reduction.

The compiled Δ^{33}S and Δ^{36}S data of detrital pyrites (with the exception of g9) are distributed along a single line for Δ^{33}S vs. Δ^{36}S (Fig. 3b). This linear correlation and slope of about −0.9 is consistently recognized in Archean rocks from various ages and localities (Farquhar et al., 2000, 2013; Kaufman et al., 2007; Ueno et al., 2008; Ono et al., 2009a; Zerkle et al., 2012; Kurzweil et al., 2013; Roerdink et al., 2013). However, distinct Δ^{33}S vs. Δ^{36}S correlations, which commonly have a slope < −1, are also observed in multiple Archean samples (Ono et al., 2006a, 2009a; Farquhar et al., 2007b; Kaufman et al., 2007; Ueno et al., 2008; Thomazo et al., 2009, 2013; Zerkle et al., 2012; Whitehouse, 2013). Changes of the Δ^{36}S/Δ^{33}S ratio could be caused by differences in the Earth's atmosphere (Farquhar et al., 2007b; Kaufman et al., 2007; Ono et al., 2009a; Zerkle et al., 2012) and the combination of the sulfur cycle in sediments and biochemical effects (Johnston et al., 2006; Ono et al., 2006b; Roerdink et al., 2013). It is likely that the Δ^{36}S/Δ^{33}S values of sulfur reservoirs that formed Archean pyrite fluctuated with time (e.g., Kaufman et al., 2007; Zerkle et al., 2012). In contrast, a tight distribution along a line with slope = −0.96 ± 0.10 of detrital pyrite grains in the glaciogenic sandstone (MB190583) suggests that these pyrite grains derived from a limited range of source rocks and near-surface sulfur reservoirs. The distribution of sulfur isotope ratios of pyrite grains (Fig. 3) is similar to those of the Lower Unit of the Mt. McRae Shale, Western Australia (Kaufman et al., 2007; Ono et al., 2009b). Sedimentary rocks formed around the same time as the Lower Unit of the Mt. McRae Shale (~2.50 Ga; Anbar et al., 2007) might be a major supply source of pyrite grains in the glaciogenic sandstone.

It is worth mentioning that two pyrite grains, g9 and g30, have distinctive sulfur isotope ratios. Pyrite grain g9 is an aggregate of multiple subhedral pyrite grains (Fig. 1f), suggesting that its formation process was different from clearly detrital pyrites with rounded margins. Sulfur isotope analyses from two spots confirmed that this grain exhibits a small excess in ^{33}S (Δ^{33}S ~ 0.60‰), which is within the range of authigenic pyrite from the rest of the section (−1 to 1‰, Williford et al., 2011), with significant deficit in ^{36}S (Δ^{36}S ~ −2.2‰) (Table 5). On the Δ^{33}S–Δ^{36}S plot, g9 deviates from the line with slope ~ −0.9 toward a slope −6.85 line (Δ^{36}S/Δ^{33}S = −3.7 ± 1.0, Fig. 3b), which is proposed to result from a combination of a mass-dependent isotope fractionation by biochemical processes and mixing of multiple isotope reservoirs (Johnston et al., 2006; Ono et al., 2006b). Its characteristic morphology and sulfur isotope ratios suggest that this pyrite aggregate is authigenic, rather than detrital, and formed by biochemical activity during, or after, sedimentation.

In contrast to g9, the rounded shape of pyrite grain g30 (Fig. 1c) indicates a detrital origin. The S-MIF value (Δ^{33}S ~ −3‰, Δ^{36}S ~ 5‰; Fig. 3) of g30, which is consistent with the observed linear trend of slope ~ −0.9, suggests that the S-MIF signature of g30 is the inheritance of a S-MIF signature of a sulfur source. However, the S-MIF signature of g30 is distinct from those of other detrital pyrite grains (Fig. 3b) and its values are opposite in sign to the expected values of elemental sulfur. The S-MIF signature of g30 may represent that of a complementary sulfate component (e.g., Ueno et al., 2008). This pyrite grain has the highly negative and variable δ^{34}S values (−32.7 to −27.4‰ within a ~70 μm pyrite grain, Fig. 6 and Table 5). Although heterogeneity of δ^{34}S value can be explained by either changes in the biological fractionation (e.g., Johnston, 2011) or Rayleigh-like processes leading to with distillation of sulfur isotopes (e.g. Kakegawa et al., 1998), a small but consistent negative correlation between δ^{34}S and Δ^{33}S in g30 (Williford et al., 2011; this study, Table 5) is consistent with the isotopic systematics of the biological fractionation. Significant mass-dependent fractionation of g30 is probably caused by bacterial sulfate reduction.

6. Conclusions

Here, we describe improved in situ sulfur four-isotope analysis techniques with SIMS by enabling simultaneous measurement with four Faraday cup detectors. A pyrite standard, UWPy-1, whose sulfur four-isotope ratios were independently redetermined with gas-source mass spectrometry in two laboratories, was used as a running standard for SIMS analysis.

Typical reproducibility (±2 SD) of spot-to-spot analyses of UWPy-1 standard with a primary beam diameter of ~20 μm were 0.23‰, 0.05‰, and 0.86‰ for δ^{34}S, Δ^{33}S, and Δ^{36}S, respectively. A slightly defocused primary beam condition that diminishes changes of $\delta^{34}S_{raw}$ and the sulfur ion yield is important to perform highly precise and accurate sulfur four-isotope analysis. In situ SIMS analysis with four Faraday cup detectors has important advantages for the study of sub-permil-level intra- and inter-grain heterogeneity of sulfur four-isotope systematics with a scale of 20 μm.

The abundance of ^{36}S relative to other sulfur isotopes measured by SIMS with both a single FC detector and multiple-FC detector settings is consistently ~19‰ lower than the estimated VCDT value (Ding et al., 2001). Our data show that the ^{36}S/^{32}S ratio of VCDT is 1 / (6641 ± 27).

Sulfur isotope systematics of detrital pyrite grains in ~2.4 Ga glaciogenic sandstone were measured by our new technique. Pyrite grains vary in sulfur isotope ratios (−32.7 to 13.5 for δ^{34}S, −3.03 to 11.66 for Δ^{33}S, and −9.7 to 4.6 for Δ^{36}S). The sulfur three-isotope data match previous results using a different SIMS method. However, sulfur isotope ratios of detrital pyrites (excluding one texturally distinct pyrite aggregate) are distributed along a line with a slope = −0.96 ± 0.10 for Δ^{33}S vs. Δ^{36}S. This relation suggests that pyrite grains mostly derived from a limited range of source rocks and a near-surface sulfur reservoir (perhaps the ~ 2.50 Ga Lower Unit of the Mt. McRae Shale). In contrast, the pyrite aggregate g9 has distinct morphology from other pyrite grains in the glaciogenic sandstone and exhibits significant deficit in ^{36}S with a small excess in ^{33}S (Δ^{36}S/Δ^{33}S = −3.7 ± 1.0), suggesting that this grain is not detrital in origin, but represents authigenic pyrite formed by biochemical activity during, or after, sedimentation. Recognition of a large negative mass-dependent fractionation (approximately −30‰ in δ^{34}S) associated with heterogeneity in δ^{34}S within a single detrital grain (g30) suggests that pyrite grains formed by bacterial sulfate reduction could have sulfur isotope zoning.

This study demonstrates that pyrite grains in sedimentary rocks could have intra- and inter-grain sulfur isotope heterogeneity because of multiple pyrite-forming processes and that in situ sulfur four-isotope analysis by SIMS resolves complex sulfur four-isotope systematics and pyrite-forming processes in sedimentary rocks with a scale of 20 μm.

Acknowledgments

We thank Noriko Kita and Reinhard Kozdon for the discussion and support for the analytical development by ion microprobe, Brian Hess for the sample preparation, Jim Kern for the maintenance of the ion microprobe, and Nanping Wu for the assistance with analyses by gas-source mass spectrometry at the University of Maryland. Comments and suggestions by two anonymous reviewers and the editor M. E. Böttcher improved the discussions.

Funding was provided by NASA Astrobiology Institute. The WiscSIMS laboratory is partially supported by NSF-EAR-1053466. KHW is supported at the Jet Propulsion Laboratory, California Institute of Technology by NASA. Sample collection was supported by the Geological Survey of Western Australia. The NSF/IF is thanked for supporting the analyses at Harvard University.

Appendix A. Supplementary data

Supplementary data to this article can be found online at http://dx.doi.org/10.1016/j.chemgeo.2014.06.006.

References

Anbar, A.D., Duan, Y., Lyons, T.W., Arnold, G.L., Kendall, B., Creaser, R.A., Kaufman, A.J., Gordon, G.W., Scott, C., Garvin, J., Buick, R., 2007. A whiff of oxygen before the Great Oxidation Event? Science 317, 1903–1906.

Barrie, C.T., Taylor, C.F., 2001. Geology, alteration mineralogy, geochemistry and volcanogenic massive-sulphide potential of the Ruttan mine area and the southern Rusty Lake volcanic belt (NTS 64B). Manitoba Industry, Trade and Mines, Manitoba Geological Survey, Open File Report OF2001-9.

Bekker, A., Holland, H.D., Wang, P.-L., Rumble III, D., Stein, H.J., Coetzee, L.L., Beukes, N.J., 2004. Dating the rise of atmospheric oxygen. Nature 427, 117–120.

Cabral, R.A., Jackson, M.G., Rose-Koga, E.F., Koga, K.T., Whitehouse, M.J., Antonelli, M.A., Farquhar, J., Day, J.M.D., Hauri, E.H., 2013. Anomalous sulphur isotopes in plume lavas reveal deep mantle storage of Archaean crust. Nature 496, 490–493.

Canfield, D.E., 2005. The early history of atmospheric oxygen: homage to Robert M. Garrels. Annu. Rev. Earth Planet. Sci. 33, 1–36.

Crowe, D.E., 1990. Geochemistry of Volcanogenic Massive Sulfide and High-grade Au Granite-hosted Ore Deposits, Southern Alaska, and, Development and Application of Laser Microprobe Techniques for Analysis of Sulfur, Carbon and Oxygen Isotope Ratios. Ph.D. thesis University of Wisconsin, Madison, WI, (209 pp.).

Crowe, D.E., Vaughan, R.G., 1996. Characterization and use of isotopically homogeneous standards for *in situ* laser microprobe analysis of $^{34}S/^{32}S$ ratios. Am. Mineral. 81, 187–193.

Danielache, S.O., Eskebjerg, C., Johnson, M.S., Ueno, Y., Yoshida, N., 2008. High-precision spectroscopy of 32S, 33S, and 34S sulfur dioxides: ultraviolet absorption cross sections and isotope effects. J. Geophys. Res. 113, D17314.

Deloule, E., Allegre, C.J., Doe, B.R., 1986. Lead and sulfur isotope microstratigraphy in galena crystals from Mississippi Valley-type deposits. Econ. Geol. 81, 1307–1321.

Ding, T., Valkiers, S., Kipphardt, H., De Bievre, P., Taylor, P.D.P., Gonfiantini, R., Krouse, R., 2001. Calibrated sulfur isotope abundance ratios of three IAEA sulfur isotope reference materials and V-CDT with a reassessment of the atomic weight of sulfur. Geochim. Cosmochim. Acta 65, 2433–2437.

Farquhar, J., Wing, B.A., 2003. Multiple sulfur isotopes and the evolution of the atmosphere. Earth Planet. Sci. Lett. 213, 1–13.

Farquhar, J., Bao, H., Thiemens, M., 2000. Atmospheric influence of Earth's earliest sulfur cycle. Science 289, 756–758.

Farquhar, J., Wing, B.A., McKeegan, K.D., Harris, J.W., Cartigny, P., Thiemens, M.H., 2002. Mass-independent sulfur of inclusions in diamond and sulfur recycling on early Earth. Science 298, 2369–2372.

Farquhar, J., Johnston, D.T., Wing, B.A., 2007a. Implications of conservation of mass effects on mass-dependent isotope fractionations: influence of network structure on sulfur isotope phase space of dissimilatory sulfate reduction. Geochim. Cosmochim. Acta 71, 5862–5875.

Farquhar, J., Peters, M., Johnston, D.T., Strauss, H., Masterson, A., Wiechert, U., Kaufman, A.J., 2007b. Isotopic evidence for Mesoarchaean anoxia and changing atmospheric sulphur chemistry. Nature 449, 706–709.

Farquhar, J., Cliff, J., Zerkle, A.L., Kamyshny, A., Poulton, S.W., Clair, M., Adams, D., Harms, B., 2013. Pathways for Neoarchean pyrite formation constrained by mass-independent sulfur isotopes. Proc. Natl. Acad. Sci. U. S. A. 110, 17638–17643.

Fayek, M., 2009. Hydrogen, carbon, nitrogen, and sulfur isotope microanalysis by secondary ion mass spectrometry. In: Fayek, M. (Ed.), MAC Short Course 41: Secondary Ion Mass Spectrometry in the Earth Sciences, pp. 65–83.

Gomes, M.L., Hurtgen, M.T., 2013. Sulfur isotope systematics of a euxinic, low-sulfate lake: evaluating the importance of the reservoir effect in modern and ancient oceans. Geology 41, 663–666.

Graham, C.M., Valley, J.W., 1992. Sulphur isotope analysis of pyrites. Chem. Geol. 101, 173–176.

Guo, Q., Strauss, H., Kaufman, A.J., Schröder, S., Cutzmer, J., Wing, Boswell, Baker, M.A., Bekker, A., Jin, Q., Kim, S.-T., Farquhar, J., 2009. Reconstruction Earth's surface oxidation across the Archean–Proterozoic transition. Geology 37, 399–402.

Habicht, K.S., Gade, M., Thamdrup, B., Berg, P., Canfield, D.E., 2002. Calibration of sulfate levels in the Archean ocean. Science 298, 2372–2374.

Heck, P.R., Ushikubo, T., Schmitz, B., Kita, N.T., Spicuzza, M.J., Valley, J.W., 2010. A single asteroidal source for extraterrestrial Ordovician chromite grains from Sweden and China: high-precision oxygen three-isotope SIMS analysis. Geochim. Cosmochim. Acta 74, 497–509.

Holland, H.D., 1984. The Chemical Evolution of the Atmosphere and Oceans. Princeton University Press, Princeton, USA.

Holland, H.D., 1994. Early Proterozoic atmospheric change. In: Bengston, S. (Ed.), Early Life on Earth. Columbia University Press, New York, USA, pp. 237–244.

Ireland, T.R., Scram, N., Holden, P., Lan, P., Ávila, J., Amelin, Y., Latimore, A., Corrigan, D., Clement, S., Foster, J.J., Compston, W., 2014. Charge-mode electrometer measurements of S-isotopic compositions on SHRIMP-SI. Int. J. Mass Spectrom. 359, 26–37.

Johnson, J.E., Webb, S.M., Thomas, K., Ono, S., Kirschvink, J.L., 2013. Manganese-oxidizing photosynthesis before the rise of cyanobacteria. Proc. Natl. Acad. Sci. U. S. A. 110, 11238–11243.

Johnston, D.T., 2011. Multiple sulfur isotopes and the evolution of Earth's surface sulfur cycle. Earth-Sci. Rev. 106, 161–183.

Johnston, D.T., Poulton, S.W., Fralick, P.W., Wing, B.A., Canfield, D.E., Farquhar, J., 2006. Evolution of the oceanic sulfur cycle at the end of the Paleoproterozoic. Geochim. Cosmochim. Acta 70, 5723–5739.

Kakegawa, T., Kawai, H., Ohmoto, H., 1998. Origins of pyrites in the ~2.5 Ga Mt. McRae Shale, the Hamersley District, Western Australia. Geochim. Cosmochim. Acta 62, 3205–3220.

Kamber, B.S., Whitehouse, M.J., 2007. Micro-scale sulphur isotope evidence for sulphur cycling in the late Archean shallow ocean. Geobiology 5, 5–17.

Kaufman, A.J., Johnston, D.T., Farquhar, J., Masterson, A.L., Lyons, T.M., Bates, S., Anbar, A.D., Arnold, G.L., Garvin, J., Buick, R., 2007. Late Archean biospheric oxygenation and atmospheric evolution. Science 317, 1900–1903.

Kelly, J.L., Fu, B., Kita, N.T., Valley, J.W., 2007. Optically continuous silcrete quartz cements of the St. Peter Sandstone: high precision oxygen isotope analysis by ion microprobe. Geochim. Cosmochim. Acta 71, 3812–3832.

Kita, N.T., Ushikubo, T., Fu, B., Valley, J.W., 2009. High precision SIMS oxygen isotope analysis and the effect of sample topography. Chem. Geol. 264, 43–57.

Kita, N.T., Huberty, J.M., Kozdon, R., Beard, B.L., Valley, J.W., 2011. High-precision SIMS oxygen, sulfur and ion stable isotope analyses of geological materials: accuracy, surface topography and crystal orientation. Surf. Interface Anal. 43, 427–431.

Kopf, S., Ono, S., 2012. Sulfur mass-independent fractionation in liquid phase chemistry: UV photolysis of phenacylphenylsulfone as a case study. Geochim. Cosmochim. Acta 85, 160–169.

Kozdon, R., Kita, N.T., Huberty, J.M., Fournelle, J.H., Johnson, C.A., Valley, J.W., 2010. In situ sulfur isotope analysis of sulfide minerals by SIMS: precision and accuracy, with application to thermometry of similar to 3.5 Ga Pilbara cherts. Chem. Geol. 275, 243–253.

Kurzweil, F., Clair, M., Thomazo, C., Peters, M., Hannington, M., Strauss, H., 2013. Atmospheric sulfur rearrangement 2.7 billion years age: evidence for oxygenic photosynthesis. Earth Planet. Sci. Lett. 366, 17–26.

Lyon, J.R., 2007. Mass-dependent fractionation of sulfur isotopes by isotope-selective photodissociation of SO_2. Geophys. Res. Lett. 34, L22811.

Martin, D. McB, 1999. Depositional setting and implications of Paleoproterozoic glaciomarine sedimentation in the Hamersley Province, Western Australia. Geol. Soc. Am. Bull. 111, 189–203.

Masterson, A.L., Farquhar, J., Wing, B.A., 2011. Sulfur mass-independent fractionation patterns in the broadband UV photolysis of sulfur dioxide: pressure and third body effects. 306, 253–260.

Mojzsis, S.J., Coath, C.D., Greenwood, J.P., McKeegan, K.D., Harrison, T.M., 2003. Mass-independent isotope effects in Archean (2.5 to 3.8 Ga) sedimentary sulfides determined by ion microprobe analysis. Geochim. Cosmochim. Acta 67, 1635–1658.

Oduro, H., Harms, B., Sintim, H.O., Kaufman, A.J., Cody, G., Farquhar, J., 2011. Evidence of magnetic isotope effects during thermochemical sulfate reduction. Proc. Natl. Acad. Sci. U. S. A. 108, 17635–17638.

Ono, S., Eigenbrode, J.L., Pavlov, A.A., Kharecha, P., Rumble III, D., Kasting, J.F., Freeman, K.H., 2003. New insights into Archean sulfur cycle from mass-independent sulfur isotope records from the Hamersley Basin, Australia. Earth Planet. Sci. Lett. 213, 15–30.

Ono, S., Beukes, N.J., Rumble, D., Fogel, M.L., 2006a. Early evolution of atmospheric oxygen from multiple-sulfur and carbon isotope records of the 2.9 Ga Mozaan Group of the Pongola Supergroup. S. Afr. J. Geol. 109, 97–108.

Ono, S., Wing, B., Johnston, D., Farquhar, J., Rumble, D., 2006b. Mass-dependent fractionation of quadruple stable sulfur isotope system as a new tracer of sulfur biogeochemical cycles. Geochim. Cosmochim. Acta 70, 2238–2252.

Ono, S., Beukes, N.J., Rumble, D., 2009a. Origin of two distinct multiple-sulfur isotope compositions of pyrite in the 2.5 Ga Klein Naute Formation, Griqualand West Basin, South Africa. Precambrian Res. 169, 48–57.

Ono, S., Kaufman, A.J., Farquhar, J., Sumner, D.Y., Buekes, N.J., 2009b. Lithofacies control on multiple-sulfur isotope records and Neoarchean sulfur cycles. Precambrian Res. 169, 58–67.

Ono, S., Whitehill, A.R., Lyons, J.R., 2013. Contribution of isotopologue self-shielding to sulfur mass-independent fractionation during sulfur dioxide photolysis. J. Geophys. Res. 118, 2444–2454.

Papineau, D., Mojzsis, S.J., Schmitt, A.K., 2007. Multiple sulfur isotopes from Paleoproterozoic Huronian interglacial sediments and the rise of atmospheric oxygen. Earth Planet. Sci. Lett. 255, 188–212.

Partridge, M.A., Golding, S.D., Baublys, K.A., Young, E., 2008. Pyrite paragenesis and multiple sulfur isotope distribution in late Archean and early Paleoproterozoic Hamersley sediments. Earth Planet. Sci. Lett. 272, 41–49.

Pavlov, A.A., Kasting, J.F., 2002. Mass-independent fractionation of sulfur isotopes in Archean Sediments: strong evidence for an anoxic Archean atmosphere. Astrobiology 2, 27–41.

Philippot, P., Van Zuilen, M., Rollion-Bard, C., 2012. Variations in atmospheric sulphur chemistry on early Earth linked to volcanic activity. Nat. Geosci. 5, 668–674.

Roerdink, D.L., Mason, P.R.D., Whitehouse, M.J., Reimer, T., 2013. High-resolution quadruple sulfur isotope analyses of 3.2 Ga pyrite from the Barberton Greenstone Belt in South Africa reveal distinct environmental controls on sulfide isotopic arrays. Geochim. Cosmochim. Acta 117, 203–215.

Thomazo, C., Ader, M., Farquhar, J., Philippot, P., 2009. Methanotrophs regulated atmospheric sulfur isotope anomalies during the Mesoarchean (Tumbiana Formation, Western Australia). Earth Planet. Sci. Lett. 279, 65–75.

Thomazo, C., Nisbet, E.G., Grassineau, N.V., Peters, M., Strauss, H., 2013. Multiple sulfur and carbon isotope composition of sediments from the Belingwe Greenstone Belt (Zimbabwe): a biogenic methane regulation on mass independent fractionation of sulfur during the Neoarchean? Geochim. Cosmochim. Acta 121, 120–138.

Ueno, Y., Ono, S., Rumble, D., Maruyama, S., 2008. Quadruple sulfur isotope analysis of ca. 3.5 Ga Dresser Formation: new evidence for microbial sulfate reduction in the early Archean. Geochim. Cosmochim. Acta 72, 5675–5691.
Valley, J.W., Kita, N.T., 2009. In situ oxygen isotope geochemistry by ion microprobe. In: Fayek, M. (Ed.), Mineralogical Association of Canada Short Course 41: Secondary Ion Mass Spectrometry in the Earth Sciences, pp. 19–63.
Van Kranendonk, M., 2010. Three and a half billion years of life on Earth: a transect back into deep time. Geological Survey of Western Australia Record 2010/21Geological Survey of Western Australia, East Perth.
Watanabe, Y., Farquhar, J., Ohmoto, H., 2009. Anomalous fractionations of sulfur isotopes during thermochemical sulfate reduction. Science 324, 370–373.
Whitehill, A.R., Ono, S., 2012. Excitation band dependence of sulfur isotope mass-independent fractionation during photochemistry of sulfur dioxide using broadband light sources. Geochim. Cosmochim. Acta 94, 238–253.
Whitehill, A.R., Xie, C., Hu, X., Guo, H., Ono, S., 2013. Vibronic origin of sulfur mass-independent isotope effect in photoexcitation of SO_2 and the implications to the early earth's atmosphere. Proc. Natl. Acad. Sci. U. S. A. 110, 17697–17702.
Whitehouse, M.J., 2013. Multiple sulfur isotope determination by SIMS: Evaluation of reference sulfides for $\Delta^{33}S$ with observations and a case study on the determination of $\Delta^{36}S$. Geostand. Geoanal. Res. 37, 19–33.
Whitehouse, M.J., Kamber, B.S., Fedo, C.M., Lepland, A., 2005. Integrated Pb- and S-isotope investigation of sulphide minerals from the early Archean of southwest Greenland. Chem. Geol. 222, 112–131.
Williford, K.H., Van Kranendonk, M.J., Ushikubo, T., Kozdon, R., Valley, J.W., 2011. Constraining atmospheric oxygen and seawater sulfate concentrations during Paleoproterozoic glaciation: in situ sulfur three-isotope microanalysis of pyrite from the Turee Creek Group, Western Australia. Geochim. Cosmochim. Acta 75, 5686–5705.
Zahnle, K., Claire, M., Catling, D., 2006. The loss of mass-independent fractionation in sulfur due to a Palaeoproterozoic collapse of atmospheric methane. Geobiology 4, 271–283.
Zerkle, A.L., Claire, M.W., Domagal-Goldman, S.D., Farquhar, J., Poulton, S.W., 2012. A bistable organic-rich atmosphere on the Neoarchaean Earth. Nat. Geosci. 5, 359–363.